Design of a velocity map imaging spectrometer for laser-gas phase atomic and molecular spectroscopy

Ritika

MS14136

A dissertation submitted for the partial fulfilment of BS-MS dual degree in Science

Indian Institute of Science Education and Research, Mohali

India

April 2019

Certificate of Examination

This is to certify that the dissertation titled **"Design of a velocity map imaging spectrometer for laser-gas phase atomic and molecular spectroscopy"** submitted by **Ms.Ritika** (Reg. No. MS14136) for the partial fulfilment of BS-MS dual degree program of the Institute, has been examined by the thesis committee duly appointed by the Institute. The committee finds the work done by the candidate satisfactory and recommends that the report be accepted.

Dr. Kamal P. Singh   Dr. Abhishek Chaudhuri   Dr. Samir Biswas

(Supervisor)

Dated:

Declaration

The work in this dissertation has been carried out by me under the guidance of Dr. Kamal P. Singh at the Indian Institute of Science Education and Research, Mohali, India.

This work has not been submitted in part or in full for a degree, a diploma, or a fellowship to any other university or institute. Whenever contributions of others are involved, every effort is made to indicate this clearly, with due acknowledgement of collaborative research and discussions. This thesis is a bonafide record of original work done by me and all sources listed within have been detailed in the bibliography.

Ritika

(MS14136)

Dated:

In my capacity as the supervisor of the candidate's project work, I certify that the above statements by the candidate are true to the best of my knowledge.

Dr. Kamal P. Singh

(Supervisor)

List of Figures

Contents

Abstract

Velocity map imaging (VMI) of photoproducts or fragments after a process of photoionization/photodissociation is a highly manifested ion imaging technique in the field of chemical and molecular dynamics which allows us to do measurements of velocity and angular distributions of the products and therefore it provides information on the various energy transfer processes. This technique is based on the use of an electrostatic lens to accelerate the ions towards a position sensitive detector. On proper adjustment of the voltages on the electrode plates, this lens has the advantage that it focuses ions with the same velocity to a single spot on the detector regardless of where the ions were created. In this thesis, I have discussed the details of the construction of such a VMI spectrometer and tried to comprehend all the nitty-gritty details pertaining to the setup. The first two chapters contain the physics and theory behind the working and building of such a spectrometer. The third chapter comprises of the simulation work concerning the design required, based on our needs and forms the foundations of the work done after that. Following this, further work involves the realisation of the simulated design on an optical bench in the laboratory and deals with a 3D model of the system. It deals with the various practical problems which could be encountered in the realization of the design. It is succeeded by the design of a molecular beam pulsed valve forming an integral part of the VMI spectrometer. The final chapter embraces a consummation of the work done till now and to be undertaken for assembling the spectrometer in the Femtosecond laser lab at IISER Mohali and realizing the goal of accomplishing attosecond XUV pulse characterization and time-domain spectroscopy.

Chapter 1

Introduction

1.1   Background

The emergence of charged particle imaging techniques has made headway to our understanding of the structure and dynamics of molecules in excited state and their gas phase reactivity. Imaging experiments provide dynamical information about gas-phase molecular reactions or atomic collisions, e.g. with the information on kinetic energy release of the reaction products; we can predict whether it is translationally or internally excited. The angular distribution of reaction products can give information about the nature of the internal excitation and whether or not the spatial product distribution is anisotropic. All these parameters furnish information about the nature of the electronic states and the potential energy surfaces controlling the elementary dynamical changes at atomic and molecular levels. The development of ultrafast laser sources has brought us closer to this goal gradually enhancing our knowledge of dynamics of excited states, bond breaking, charge transfer in gas phase reactions[AH 00]. The research now has been extended to the attosecond time domain, i.e., the natural time scale of electronic motion inside atoms with the advent of attosecond laser pulses providing unique possibilities for the inquiry and control of electronic degrees of freedom.

1.2 Motivation

In the presence of strong laser fields, atoms and molecules undergo a ubiquitous reaction where part of the electron wavefunction tunnel ionizes and later recombines back to the atom, driven by the laser field. The investigation of various parameters such as angular distribution and kinetic energy release associated with the emission of these electrons or the high harmonics generated by the recombining electron can lead to potential in-situ probing of the electronic orbital dynamics and hence, providing information related to the structural and dynamical behaviour of atoms and molecules under investigation.

1.3 Imaging molecular dynamics

Imaging of the atomic structure of matter, whether it is static or dynamic, has always remained at the forefront of research in physics, chemistry and biology. The advancement of ion and electron imaging techniques, in conglomeration with velocity map imaging techniques, has initiated a new generation of experimental methods to explore atomic and molecular dynamics. It has facilitated the studies of photoelectron momentum spectroscopy, molecular photodissociation and reaction dynamics, and attosecond spectroscopy[MF 08] in association with the advent of attosecond light sources. The first experimental demonstration of two-dimensional imaging of the process of photodissociation using a single laser pulse was shown by Chandler and Houston in 1987[Chandler 87] via an experiment performed on CH_3I. They first presented a technique in which they projected the three-dimensional spatial distribution of a photofragment, measured at a set time after photodissociation, onto a two-dimensional surface determining both the angular and speed distribution of the photofragments simultaneously. Since then, expeditious progress has been experienced in the conceptual and technological framework of the imaging techniques, and the improvements have led to a large number of wide applications in the field. A breakthrough in this establishment of imaging techniques was provided by Eppink and Parker[Eppink 97] who demonstrated the application of electrostatic lenses to give a substantial improvement of two-dimensional ion/electron imaging techniques.

1.4 Velocity map imaging

Previously, grid electrode setups were in use to accelerate the ions forming homogeneous electric fields and performing time-of-flight(TOF) measurements, but grid electrodes lead to a reduction in transmission, critical deflections in trajectories and blurring due to the non-point source geometry. The shaped field contours provided by the electrostatic immersion lens used in VMI help to efficiently reduce the blurring of ion/electron images that exists in using these homogeneous fields due to a finite source volume. In contrast to the conventional TOF method where kinetic energy
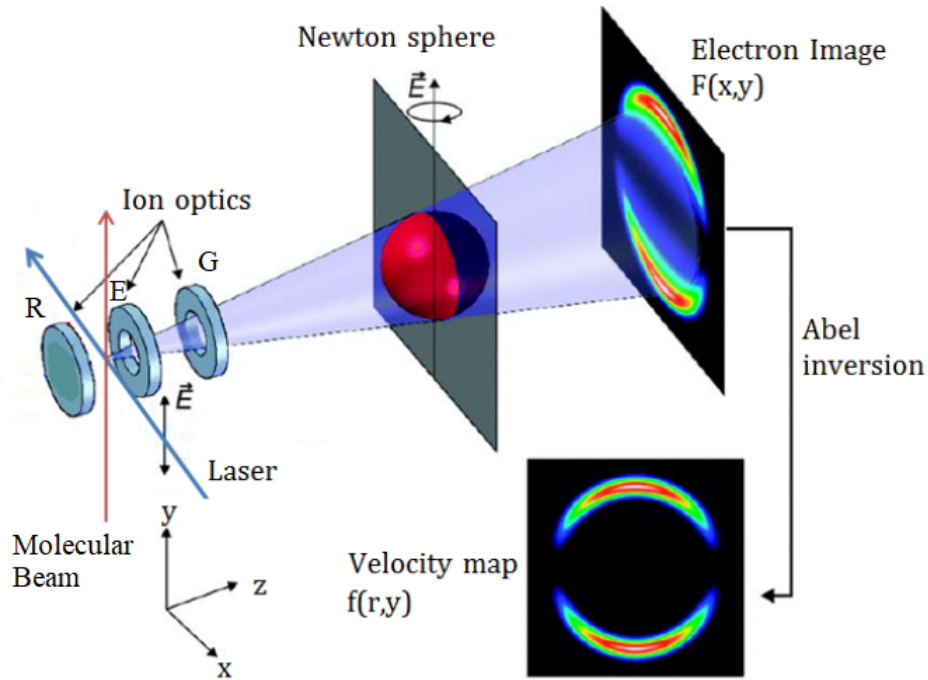
Figure 1.1: *Setup of a VMI Spectrometer*: A laser ionizes atoms located between the electrodes (R: Repeller electrode plate, E: Extractor electrode plate, G: Grounded electrode plate).The electrodes accelerate the charged particles towards a detector. On their way, they expand on a Newton sphere because of their kinetic energy. This spherical distribution is projected onto the 2D position sensitive detector surface. The initial velocity distribution can be obtained via so-called Abel-inversion process[Wituschek 16].

release information is contained in the temporal structure in the arrival period of ions or electrons of a specific mass, here all the information(kinetic energy and angular distributions) can be extracted from the spatial appearance of the 2D image. Compared to other detection techniques, it also possesses the advantage of having high collection efficiency. The ions imaged on the 2D detector reflects the recoil speed and

direction of the scattered molecules. Imaging directly reveals the differential state-to-state scattering cross-section, i.e., the "Newton sphere" which forms the basis for delineating the physical and chemical change on the microscopic level.

For the construction of such a spectrometer, we need to see through all the technicalities pertaining to the setup and a thorough understanding of all the requirements is necessary before planning. A short description of all the requirements is given in the next section.

1.5 Overview of the setup

1.5.1 Hardware Part

1. **Outer chamber design**: Chamber in which VMI is to be placed for operation. It requires a vacuum pump as all the experiments which would be performed demand strict vacuum conditions for their operations. This is necessary for ensuring a long mean free path for the electrons/ions and to avoid collisions on their way to the detector to avoid trajectory deflections. Collision number is needed to be kept as low as possible; otherwise, they can change the initial energies and distribution of the electrons. Constant vacuuming of the chamber is also important for sucking up unwanted particles (unionized particles, ions in the study of electrons and vice-versa) that may result in high noise on the imaging plate.

2. **Main core design**

   - Thin electrode plates to create immersion lens conditions. The material should have high conductance and low reactivity. Stainless steel offers an ideal choice for this.

   - Caging of the electrodes (requires bushings and standing rods) and supporting them inside the chamber.

3. μ **- metal shield**: For shielding the chamber from stray/external magnetic fields which could deflect the ion trajectories.

4. **Gas jet**: A good gas injection system is required to get a better image resolution. The desired conditions are a pulsed valve to supply smaller amounts of gases and supersonic cooling of the gas beam to reduce the spread in the initial velocity of the parent molecules.

5. **Detector**

   - Micro-channel plate (MCP) and Phosphor Screen: A MCP detector is used as a position sensitive detector to permit image visualization. The ions hit the MCP detector, it multiplies the number via the application of a strong electric field following secondary electron emissions in different MCP channels and later feeds the output to a phosphor screen which gives a visual picture of the position of the ions on the detector plane. The current available MCP in the lab is a CF150 flange mounted with a diameter of 75 mm.

   - CCD Camera: A fast CCD camera which can take pictures with high frequencies and smaller image integration times is needed along with an MCP.

6. High Voltage Power Supplies: To separate power supplies for both repeller and extractor plates are required. Should have very low noises and greater stability.

7. **Accessories:**

   - Gate Switch

   - Feedthroughs

   - Connectors

1.5.2   Software Part

1. **Simulating the design**

   The foremost part of the construction of VMI is to get an idea of the dimensions and working energy range, resolution obtainable etc. using a simulator to simulate the experimental parameters and get an understanding of the working.

For this purpose, we have used SIMION software, a detailed overview of which is presented in Chapter 3.

2. **Image acquisition and analysis**

The spectrometer needs to be calibrated first keeping in mind the available working space and image parameters. Once this is done, we can directly analyse the 2D images obtained from the camera to obtain full 3D information of the velocity distributions. This is done via various iterative algorithms integrated with the data output, or the images can be analysed afterwards also, using a mathematical transformation process known as Abel inversion. The process is described below:

Abel Transformation: The forward Abel transform is used to get a projection of 3D axial symmetric cylindrical distribution onto a plane parallel to the axis of symmetry. It is described by the given equation-

$$A(z,x) = 2 \int_x^\infty F(z,r) \frac{r\,dr}{\sqrt{r^2 - x^2}} \tag{1.1}$$

Here, z is considered as the axis of symmetry and A(z,x) is the image or projection with F(z,r) as the velocity distribution by velocity map, r is perpendicular to z.

The map F(z,r) can be calculated from the image A(z,x) by the inverse Abel transform

$$F(z,r) = -\frac{1}{\pi} \int_r^\infty \frac{\partial A}{\partial r} \frac{dx}{\sqrt{x^2 - r^2}} \tag{1.2}$$

The equation is solved using Abel inversion algorithms available for this purpose numerically because of discontinuous data points due to the finite number of pixels in CCD. The experimental data is analyzed using a few of them for comparison to find the most suitable one for the given data set and a brief description regarding them is given below.

Inverse Abel transformation methods

(a) **BASEX:** It uses a Gaussian basis set to provide a robust transform but is

computationally intensive. The basis set is a sum of functions which have known Abel inverse whose generation can take some time. However, once calculated these basis sets are stored on the disk for future use and the transformations proceed very quickly for later times. No contribution to noise is made in the reconstruction process[et al. 02].

(b) **Hansen-Law:** This recursive method by Hansen and Law is one of the fastest methods for both forward and inverse Abel transformations, but it requires fine sampled data to provide agreement with the analytical results. This provides low centerline noise[Hansen 85].

(c) **Onion-peeling:** This is also known as back-projection. It is a way of recording the suitability of the pixels of a given image to fit in the distribution of pixels in a histogram model. It determines the contributions to the signal in a given pixel (in a row), of particles with a kinetic energy. The difference is then taken and the process is repeated until a fine image is obtained. It is a simple and computationally efficient method but has less smoothing than other methods[Dasch].

(d) **Direct:** In this method, direct integration of the Abel transform integral is attempted, and thus it requires fine sampling to converge. Works well for finely sampled smooth functions but generally not found reliable for inverse Abel transformation[Dasch].

Chapter 2

Theory

2.1 Ion Optics

In ion optics, electrostatic and/or magnetic forces are used to alter charged particle trajectories. Here I will discuss the effect of electrostatic forces on charged particles only as electrostatic lensing constitutes the main principle behind the construction of a VMI spectrometer.

The force on a charged particle in an electric field is given by,

$$\vec{F} = q\vec{E} \tag{2.1}$$

where, q is the charge on the particle and $\vec{E}$ defines the electric field experienced by the charged particle. From this we can calculate the acceleration/movement, $\vec{a}$, of the particle of mass m, under the influence of an electrostatic force as

$$\vec{F} = m\vec{a} \implies \vec{a} = q(\vec{E}/m) \tag{2.2}$$

Refraction in Ion Optics

The bending of ion trajectories or refraction in an electric field is dictated by the normal component of ion's velocity to the electrostatic force. Following this, the

radius of refraction for a charged particle in an electrostatic field is calculated as

$$\text{Normal electrostatic force} = \text{Centripetal acceleration}$$

$$qE_n = mv^2/r_n \implies r_n = mv^2/qE_n \implies (m/q)v^2/E_n \tag{2.3}$$

It states that the electrostatic radius of refraction is proportional to the ion's kinetic energy per unit charge. This means that all ions with the same starting point, direction, and kinetic energy per unit charge would be having identical trajectories in electrostatic fields. These trajectories are **independent of masses** in electrostatic fields.

Light optics vs ion optics

If we compare these two frameworks, we get several similarities as well as differences regarding their underlying principles and composition. The *similarities* between ion optics and charge particle optics includes the following: The first one to note is that light traversing between two different media experiences trajectory deflection due to change in refractive indices of both the media (n_1, n_2). This relationship between the refractive indices of these two media with the angle of incidence (α_1) and refraction (α_2) of the light wave is described by Snell's law as:

$$n_1 sin(\alpha_1) = n_2 sin(\alpha_2) \tag{2.4}$$

In charged particle optics too, particles get accelerated or decelerated, when moving from one potential region to other (V_1, V_2) and the trajectory will depend on the angle of incidence with respect to the equipotential surfaces of the field. Therefore, it is hard to construct an electrostatic lens with smaller aberrations. Analogous to Snell's law, we have a refraction law here also, given by:

$$\sqrt{V_1} sin(\alpha_1) = \sqrt{V_2} sin(\alpha_2) \tag{2.5}$$

The *differences* comprise of the following:
In light optics, refractive index changes abruptly on the surface separating two media. There are smaller optical aberrations, which can be controlled or rectified one way or

the other. While in ion optics the change in velocity of a beam of charged particles varies continuously across an electrostatic lens. Thus an electrostatic lens always works as a thick lens. It deals with larger aberrations and repulsive Coulomb forces among the beam particles. Also, the difference lies in more general use of ion optics to focus a paraxial beam (i.e., particles moving mainly close and along the optical axis) onto a target point.

For conventional ions optics, *spherical* and *chromatic* aberrations refer to the notion that the particles with different initial velocity angles with respect to the optical axis and different initial speeds are not exactly mapped on one point, but on a disk in the image plane. In VMI, however, we need the mapping to be such that different angles and speeds appear on different points on the image.

2.2   Theory of Photoionization

The understanding of the process of photoionization is necessary for able to be in a position to discuss VMI It is a physical process which forms an ion after a photon interacts with an atom or molecule. It is the result of excitation or removing of their electrons. We can induce dissociation of a quantum-state selectively by exciting a molecule or cluster with laser light. The excess energy delivered by the photon above the dissociation threshold is divided between the internal energies of the daughter particles formed and their kinetic energies. This can be written in mathematical form as:

$$E_{parent} + h\nu + D_0 + E_{frag} + E_{cofrag} + KER_{total} \tag{2.6}$$

Here, E_{parent} is the parent's molecule energy, $h\nu$ is the energy delivered by the photon, D_0 is the bond dissociation energy required by the molecule, E_{frag} and E_{cofrag} are the energy of the daughter fragments with their kinetic energy release given by KER_{total}.

These nascent products expand on a "Newton sphere" which is defined by the energy and momentum conservation laws involved in the photodissociation process. These Newton spheres get collapsed on the 2D detector plane, thus forming circular images. The bond dissociation energy (D_0) can be found by measuring the radial distribution of photofragments in an image and using the corresponding transverse velocity

distribution to derive that total kinetic energy release. VMI allows us to take such pictures which give information regarding the velocity and angular distribution of the photofragments. We can also measure the relative probabilities of various dissociation channels if more than one product channel has been accessed. As a result of molecular dissociation and measuring how the energy that is released into the resulting fragments, provides a detailed probe of the nature of chemical bonds and the dynamics of chemical change.

Furthermore, anisotropy in the photofragment image of a linear molecule is dependent upon three factors:

1. The orientation of the principal molecular axis relative to the direction of photolysis laser polarization.

2. The orientation of the relevant transition dipole moment

3. The excited molecule's dissociative lifetime.

For dissociative events that occur faster than the parent's rotation timeframe, a parallel transition yields a photofragment image with greater intensity along the axis that is parallel to the laser polarization vector. Correspondingly, excitation of a perpendicular transition produces an image with intensity along the axis perpendicular to that of the polarization vector.

The intensity distribution of an image is fit to the following equation:

$$I(\theta) = \frac{1}{4\pi}[1 + \beta P_2 cos(\theta)] \tag{2.7}$$

where, θ denotes the angle between laser polarization vector and given radial position on the image, $P_2 cos(\theta)$ is second order Legendre polynomial and β is the anisotropy parameter, where $-1 \leq \beta \leq 2$. $\beta = -1$ indicates perpendicular transitions, $\beta = 2$ signifies parallel transitions and $\beta = 0$ denotes isotropic angular distribution which occurs if the lifetime of the excited state produced is longer than the rotational period of molecule.

The angular distribution measurement can provide a clear picture of the symmetries of the negative ions states that are involved, and the kinetic energies provide the

energies and dynamics of the dissociative electron attachment process.

2.3 VMI Theory

The advantage of VMI is its ability to provide the angular distribution in the entire 2π angle with respect to the particle beam as well as the kinetic energy of detected ions. This information of the velocity of the particles (angular distribution and kinetic energy) is contained in the 2D images obtained via the detector. The position of the
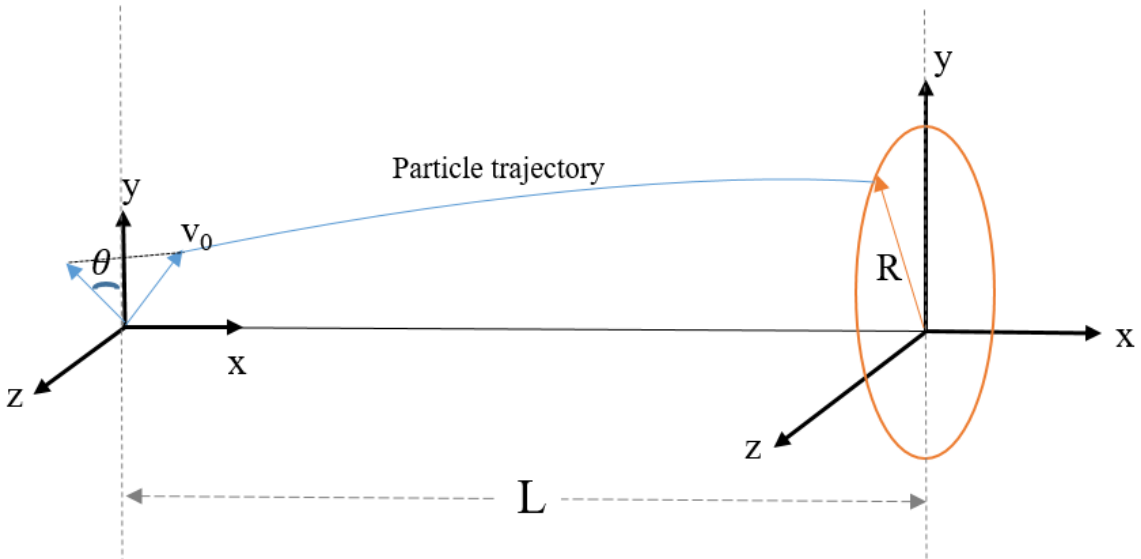
Figure 2.1: Schematic view of the geometry of the imaging

particle when it strikes the detector is directly proportional to the particles an initial velocity in the yz-direction and comprises of a magnification factor in itself due to the presence of electric fields in the yz-direction. As mentioned in the previous section, this collapse of the expansion cloud of the particles forms a ring on the detector of radius R, associated with the expansion speed, v_0 of the particles as $R = v_0 t$, where t is the time-of-flight of the given particle.

The velocity of the particle in the x-direction is given by

$$v_x = \sqrt{\frac{2K}{m}}$$ (2.8)

due to the presence of electric field which gives the kinetic energy as,

$$K = qV \tag{2.9}$$

where q is the charge on the particle and V is the acceleration potential. Neglecting the electric field in the yz-direction for the time being and assuming that the acceleration region is small compared to the total length of the spectrometer L, the time-of-flight can be approximated as

$$t \approx \frac{L}{v_x} = L\sqrt{\frac{m}{2qV}} \tag{2.10}$$

This gives the relation between the radius R and initial kinetic energy of the particle as

$$R \approx L\sqrt{\frac{K_0}{qv}} \tag{2.11}$$

where $K_0 = mv_0^2/2$. Although, due to the effect of electric field component in the yz-direction, the image appears a bit larger as it contributed by a magnification factor N from this. So, the radius of the rings on the image is given by

$$R = NL\sqrt{\frac{T_0}{qv}} \tag{2.12}$$

This magnification factor is determined via a calibration for each experimental setup and thus measuring the radius R of the images. We can determine the kinetic energy T_0 of the particles using the spectrometer.

Along with this, as discussed earlier, we can gain angular distribution information. But we cannot obtain the complete momentum information from the raw 2D VMI image data itself, as that is a projection of the 3D Newton sphere onto the 2D detector plane. Therefore, the raw data obtained from VMI spectrometer is made to undergo a mathematical transformation called inverse Abel transformation to reconstruct a slice of the cylindrically symmetric 3D photomomentum distribution. The use of a linearly polarised laser imposes the needed cylindrical symmetry to perform inverse Abel transformation due to the vector correlation relationships mentioned in the previous section, between the photoelectron angular distribution and laser polarization[Thorin 04].

Chapter 3

Simulations

A three-electrode geometry was chosen to keep the design simple with little complexity in integration at later stages minimal as it can provide a good resolution in the working energy range, i.e., $< 40eV$. The first step forward towards the realization of the project was to simulate this three-electrode VMI configuration to test for its applicability in the lab scenario. The simulations are done using SIMION 8.0 software. It is an ion and electron optics simulator to get an understanding of the design, working and knowledge of the optimum voltages for the spectrometer. VMI's expected energy range and resolution were also determined by performing trajectory simulations of charged particles.

3.1   Simion 8.0

The SIMION® is a software program for performing charged particles optics simulations. Typically, it calculates 2D/3D electrostatic and certain magnetic fields and calculates the trajectories of charged particles through those fields. It provides a programming, visualization, and data recording environment for these simulations. It includes finite difference methods and Runge-Kutta for solving basic partial differential equations (PDEs), specifically the Laplace Equation, and ordinary differential equations (ODEs) respectively. We can define the geometry via multiple methods[D. Manura 08].

3.2 VMI spectrometer

The basic workflow diagram of SIMION utilized in configuring the VMI spectrometer is as follows:

Define Array Size	Modify geometry	Refine Potential Arrays	Fly Particles	Opti-mization
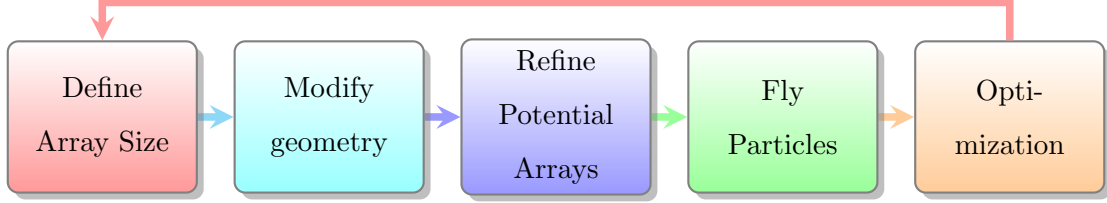
The parameters considered while performing the simulations are categorized as follows:

1. *Control parameters*: Those parameters which need to be fixed from the beginning and couldn't be modified as per the system requirements. Maximum input voltage(i.e., 5 kV) and detector size(as per their availability in the lab), along with the flight tube length which should keep as large as possible to integrate ion/electron T.O.F measurements belong to this category.

2. *Variable parameters*: Those parameters which can be varied in order to gain maximum energy resolution for the given system requirements. These include distance between electrodes, electrode/aperture sizes, shape of the electrodes/apertures and the ratio of voltages on the extractor and repeller plates(i.e., V_E/V_R) which is one of the key parameters in deciding the focusing conditions of the lens.

3.2.1 Defining the simulation in SIMION 8.0

A step-by-step guide:

Geometry definition: At first the system dimensions were defined in a "New" file in accord with the dimensions of the available chamber space shown below regarding the present attosecond setup and the system geometry was defined using an interactive 3D paint like program called "Modify". Here you model the requisite electrode shapes and sizes.

Once you create a "New" file and "Modify" it according to your needs, you need to "Save" the file name with ".pa#" extension. This file extension tells SIMION that

this is a fast adjust definition file. The next task is to "refine" the potential array (solve for the electrostatic fields).
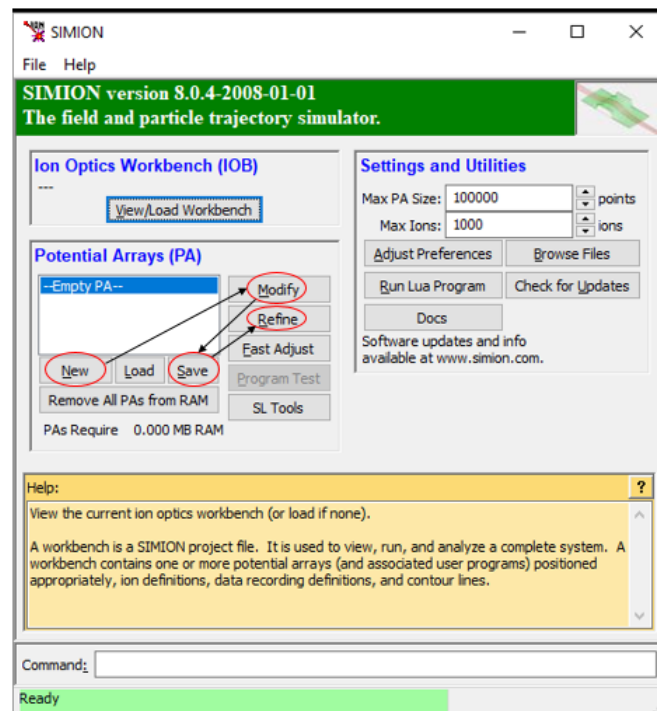

Figure 3.1: Working with SIMION

Next, you click "View/Load Workbench button" to enter in the workbench area where you can "Fast adjust" your potentials, "define particles" and their various parameters such as position, direction, speed, angular distribution, kinetic energy etc. You may define individual particles or "grouped" ones. Then you "fly" particles and see the trajectories of motion in the given potential array.

3.2.2 Simulations

I started with the bench-marking of the software using some published simulations in forefront papers[Eppink 97, Kling b] and compared the resolution of my simulations with their theoretical attained values. The results were in good accord with the previously mentioned values. After that, I started working with various parameters pertaining to our system as mentioned above and kept on checking for the best resolution conditions for each of it.

First of all, with some fixed arbitrary electrode size (a calculated guess in accord with

the VMI chamber dimensions shown below, say 12 cm in diameter), arbitrary sizes for the electrodes apertures were chosen, while varying only the distances between the electrodes at relatively large steps (2-3 mm per step). The size assumed here is in accord to the dimensions of the available chamber space, which is kind of a cylindrical one which is having a diameter of 20 cm. So, with leaving some margin nearby the walls for its placement, space to pass the wire connectors along the walls and space for placing a μ-metal sheet around the electrode plates, 12 cm fits well for the assumption.
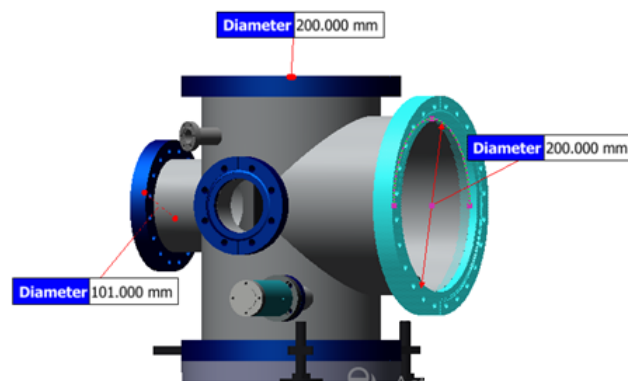

Figure 3.2: VMI chamber dimensions

The same procedure was employed by varying the sizes of the apertures and keeping the distances between the electrodes at some arbitrary fixed value, and the best resolution size was sought.

The results were analyzed to yield the most promising geometrical configuration of the whole assembly.

Subsequently, the procedure was repeated by varying the distance between electrodes at smaller steps (1 mm per step, least count for SIMION geometry definition array) for the best gap obtained out of the just above-mentioned process while keeping the best electrode aperture sized obtained in the previous step. The same was done by varying the sizes of the electrode apertures.

This process was repeated until an optimal configuration was found under a pre-set criterion of focusing.

Following that, the next parameter taken under consideration was the ratio of voltages

on the extractor plate and the repeller plate, i.e., V_E/V_R. This too was varied at smaller steps and checked at different repeller voltages. A lower repeller voltage can improve the energy resolution for low energy electrons/ions. To image electrons/ions with higher kinetic energies, higher magnitude of the repeller voltage is required. This is because of the limitation of the immersion lens created which gives us a focusing disc in the image plane, for which we get the best resolution near the selected energy value or energy range of interest and the resolution starts decreasing for higher or lower kinetic energies from the chosen range. The whole procedure of seeking the best out of the pool is repeated until the final configuration was achieved selecting to get the best focusing conditions near 40 eV previously which was later changed to 10 eV due to energy limitation put forth by order of harmonics we are able to generate. Moreover, we can control the focal distance of the image by changing the ration of V_E/V_R where as image size can be adjusted using V_E

The maximum photon energy that can be produced with high harmonic generation is given by the cut-off of the harmonic plateau. This is calculated classically by investigating the maximum energy that can be gained by the ionized electrons in the electric field of the laser. The cut-off energy is given by,

$$E_{max} = I_p + 3.17U_p \tag{3.1}$$

where U_p is the ponderomotive energy from the laser field and I_p is the ionization potential[10. 1].

So, at present, the highest-order harmonic achieved is harmonic 29, which corresponds to an energy of 45 eV. So, if argon is used to act as a carrier gas, the ionization potential of argon is given by 14.75 eV. Therefore, the range of energy interest remains 0-25 eV, for best focusing conditions to be achieved near 10 eV.

Previously, while beginning, I fixed some of the parameters like maximum repeller voltage to be used as 10 kV to focus particles of energies upto 80 eV, being hopeful of achieving this energy range while increasing the high-order harmonic generation cut-off in nearby future. A standard 3-electrode VMI design made keeping this conditions in mind and with an energy resolution of 0.2% around 40 eV is shown in Fig:3.3.
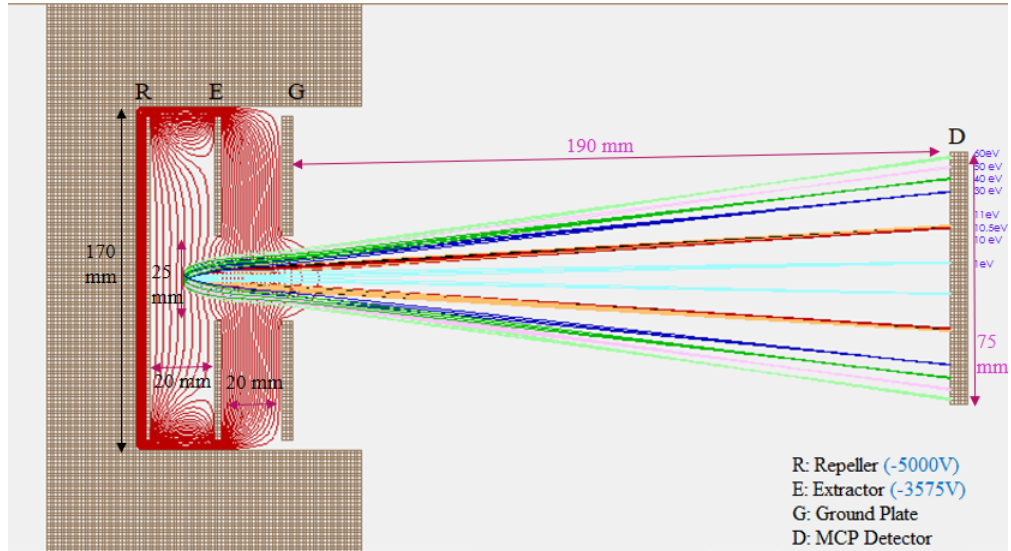
Figure 3.3: A standard 3-electrode VMI design

SIMION also provides the potential energy surface view of the potential array. Here, you can see a particle beam trajectory converging or diverging according to the potential difference slopes you have defined while working.
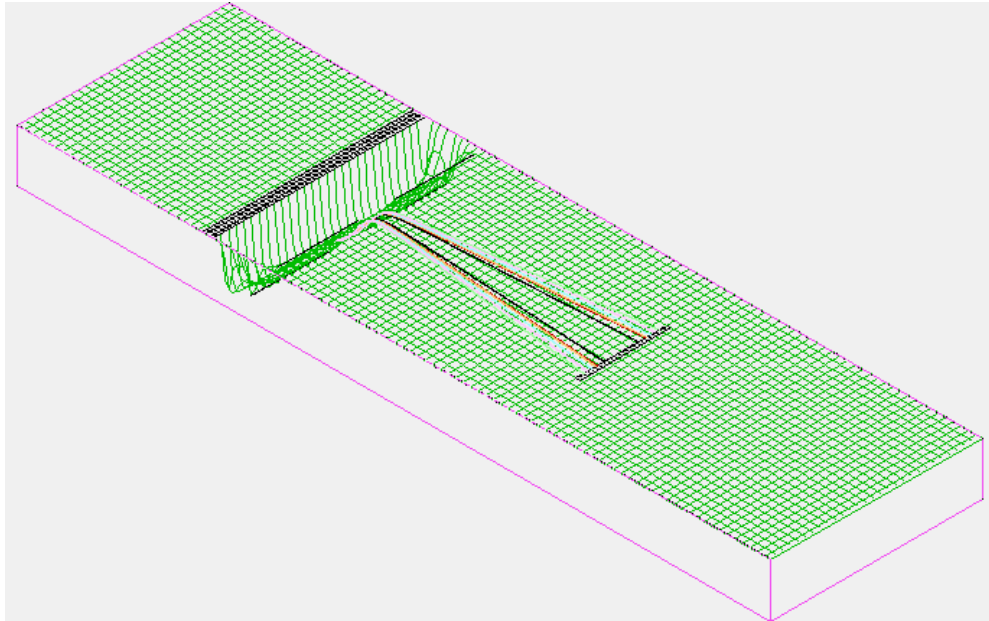
Figure 3.4: Potential energy view of potential array using the PE View function

Here, I have tried to keep the drift tube length (distance from the ground electrode to the detector) as maximum for the given geometric conditions to implement time-of-flight measurements along with VMI measurements. A drift tube length of 19 cm as shown in Fig.3.3 would work well for ions time-of-flight measurements with the use of a fast gate switch and a fast response detector with an oscilloscope. A fast high gate

19

switch along with a delay generator is used to time gate the MCP-phosphor voltage. The gate width of a few hundred ns is set at the desired delay to collect ion fragments with a specific mass-to-charge ratio selectively. In the case of electron acquisition, this switch would help to keep low background counts. Although, this flight length would not be suitable to measure electron time-of-flight with a good resolution.

3.3 Playing with SIMION

The first part of this project was to work with SIMION, to get an understanding of the design, working and knowledge of the optimum voltages for the spectrometer. Its expected energy range and resolution were also determined by performing trajectory simulations of charged particles in the confined standard geometry of using plane circular electrodes and apertures to get an image disk on the detector plane with different energies focused with different resolutions. After building up a standard 3-electrode design model in SIMION, I tried to play with the key VMI parameters which determine how good your focusing would be, in order to get a good energy resolution.

So, first of all, I chose the shape and size of the electrodes to be varied to see the difference on the image resolution as these parameters are the primary ones that dictate the energy resolution apart from others such as voltage ratios etc. A combination of circular and square electrodes and apertures were tested and analyzed for their resolution. Doing this, the perception was that the potential field contours percolating themselves through circular apertures previously, which give rise to the immersion lens condition here in ion optics similar to a spherical lens in light optics are a cause of so many aberrations. The primary motivation for this type of studies was correcting for these charged particle optics aberrations such as image curvature, astigmatism, spherical aberrations etc. which are more pronounced in charged particles optics as mentioned in Chapter 1.
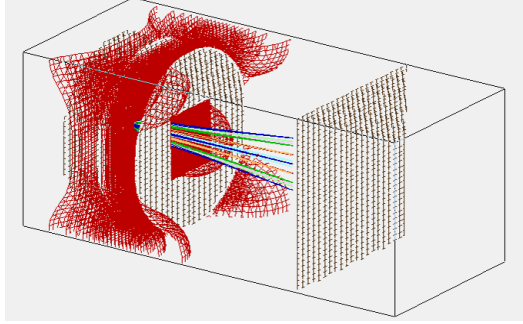
At first, a combination of different aperture shapes with sizes was investigated. The contour field planes and their percolation are shown in the SIMION images in Fig.3.5

It was anticipated that the percolation of equipotential surface contour planes through
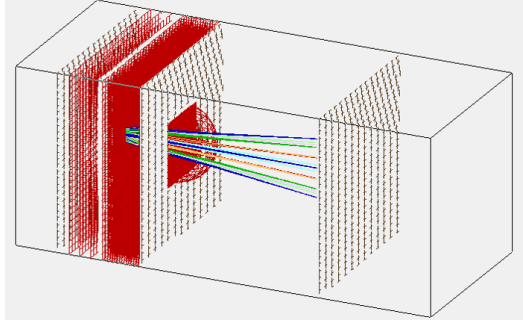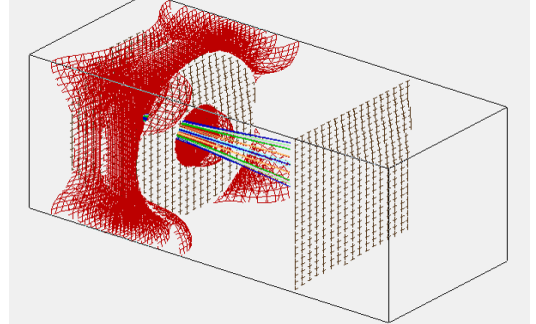
(a) Square electrodes with square apertures
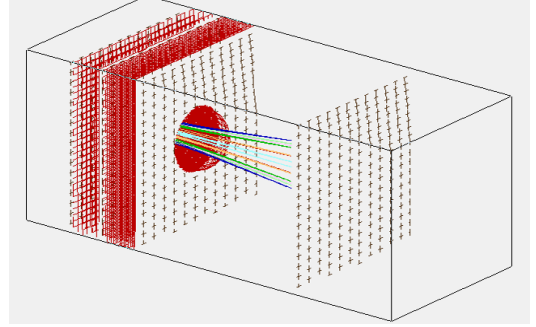
(b) Square electrodes with circular apertures

(c) Circular electrodes with square apertures

(d) Circular electrodes with circular apertures

Figure 3.5: Immersion lens creation with a combinations of circular and square shapes of apertures and electrodes

a square aperture would constitute a hyperbolic lens configuration and could improve the resolution more. Along with this as seen in the images, with square electrodes, we can see that the field doesn't spread in the entire region through edges which is the case for circular electrodes. But contrary to our expectations, an energy resolution study didn't go with these interpretations. A comparison of energy resolutions for all the four cases is shown in Fig. 3.6. It is calculated using equation (2.12) as

$$R \propto N\sqrt{E/qV_R} \implies \frac{\Delta E}{E} = \frac{2\Delta R}{R} \times 100\% \tag{3.2}$$

Here, as a concluding remark, we can see that the shape of the electrodes can be varied deliberately in order to achieve a higher resolution (eg. in the above simulations, for the energies 40 eV circular electrode rings are more effective whereas for energies 40 eV squared ring electrodes are better).

Afterwards, an attempt was made to distort the symmetrical lens formed from the same kind of ground and extractor apertures with the same diameter. An asym-
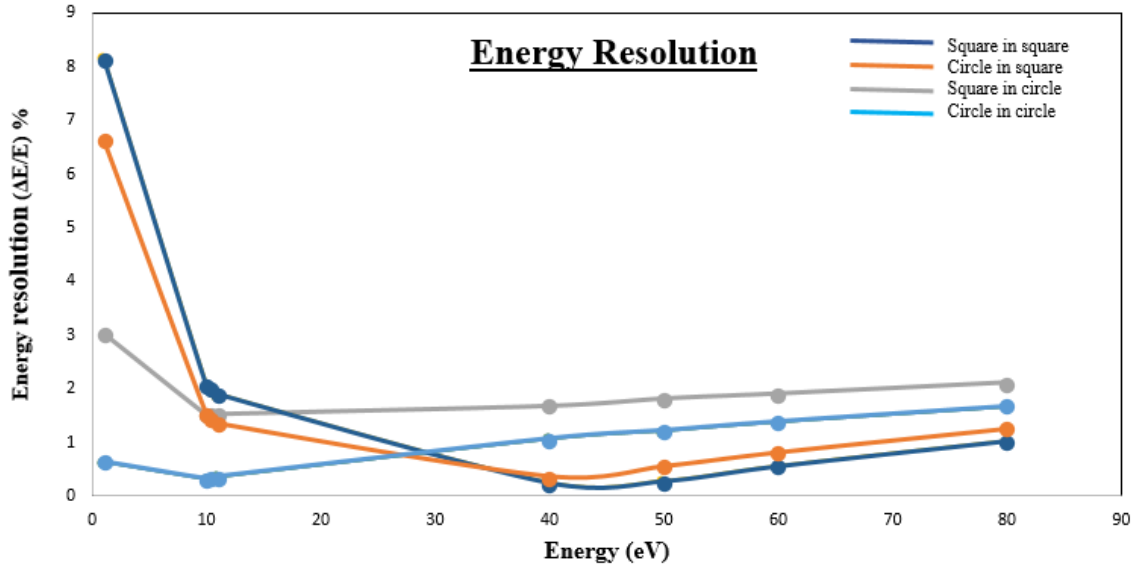
Figure 3.6: Comparison of energy resolution for a combination of electrode and aperture shapes

metrical or non-spherical lens with a complex surface profile can lower or eradicate spherical aberration and also help in correction of other optical aberrations such as astigmatism, compared to a simple spherical lens. This was done by keeping the extractor and ground aperture sizes at a particular ratio as shown in Fig.3.7.

This variation of aperture ratios for extractor and ground resulted in different kinds of lens conditions for the particles. The symmetrical apertures condition make a spherical immersion lens for the particles, whereas when we make the extractor aperture a bit wider compared to the size of the ground aperture, we saw that it created a plano-convex lens for the charged particles formed in the interaction region if the extractor aperture is made quite large. This condition improved the energy resolution of the focused images as well and created tight focusing conditions compared to the symmetrical conditions. This might be due to the inter-penetration of the repeller and extractor fields, and the particles were only accelerated from their origins initially, similar to as done in time-of-flight measurements. As the particles moved out of the initial acceleration field and entered in the extractor and ground field, then only they experienced the curvature of the field lines which modulated their trajectories and segregated them in groups based on their energies and velocities. These groupings undergo refraction based on their energies, thus traversing different curvatures. However, the resolution was decreased for the case of a wider ground aperture. This might
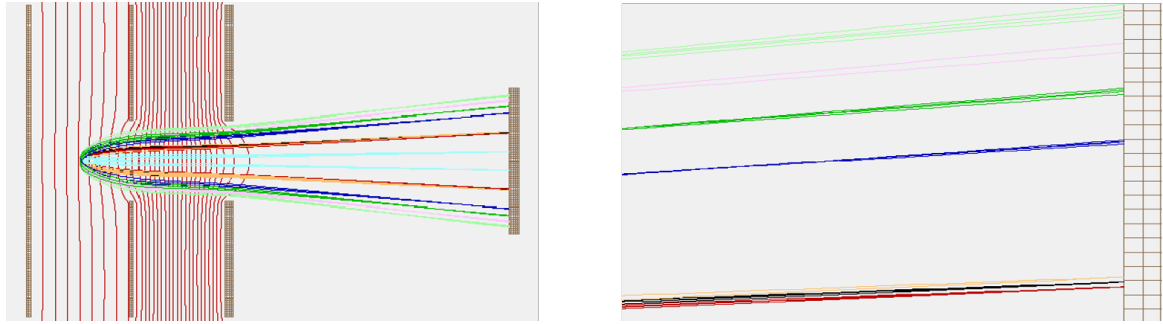
(a) Symmetric immersion lens
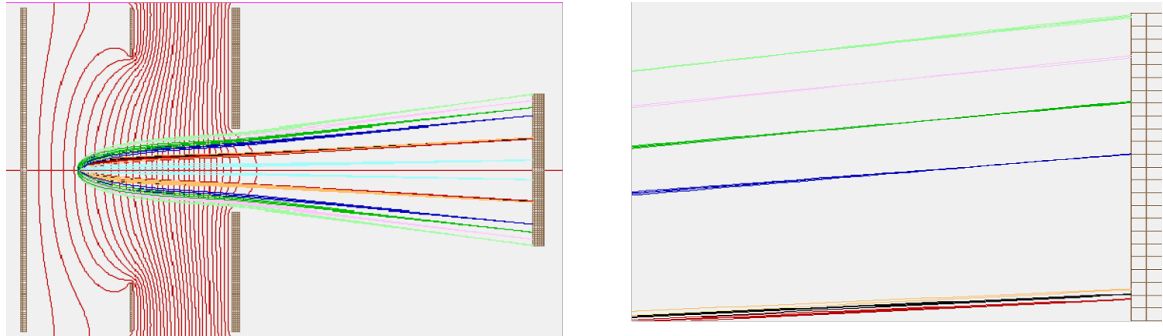
(b) Wider extractor aperture diameter
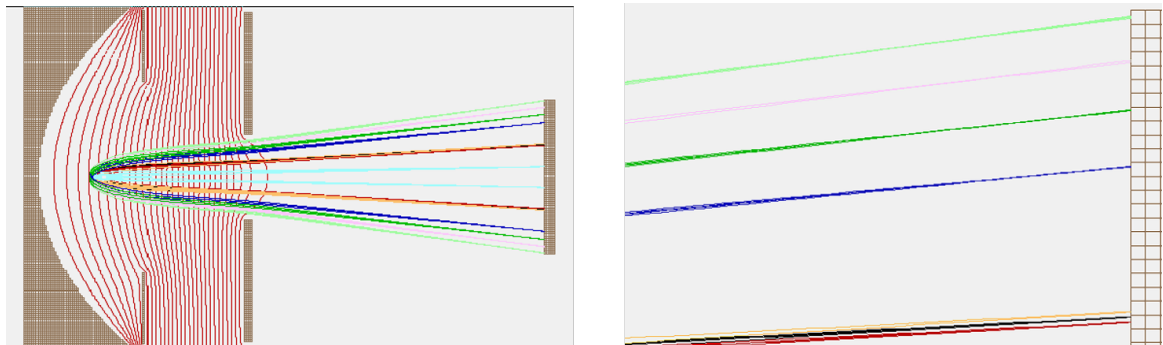
(c) Curved repeller plate
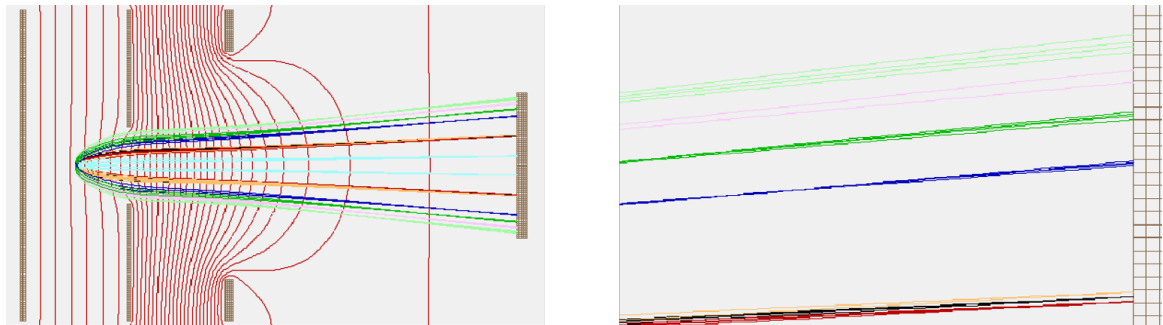
(d) Wider ground aperture diameter

Figure 3.7: Immersion lens creation with unequal apertures to create asymmetrical lenses (the second image in all the above images is a zoomed one at the detector surface at the trajectories striking points)

be due to the leaking of the electric fields in the drift region and greater curvature of field lines experienced by the particles on their exit from the lens. Later on, instead

of using a plane surface for the electrodes, I used a curved repeller plate to make the plano-convex lens condition as seen with the wider extractor aperture, more prominent to enhance the focusing further. It did improve the resolution a little bit, but not by a larger amount as shown in Fig.3.8.

Figure 3.8: Comparison between aymmetrical lens conditions

Therefore, we can say that this kind of immersion lens can be corrected for lens aberrations such as image curvature and spherical aberrations by modifying the potential field in an asymmetric manner by using curved electrode plates or keeping the inner diameter for extractor and ground plates different.
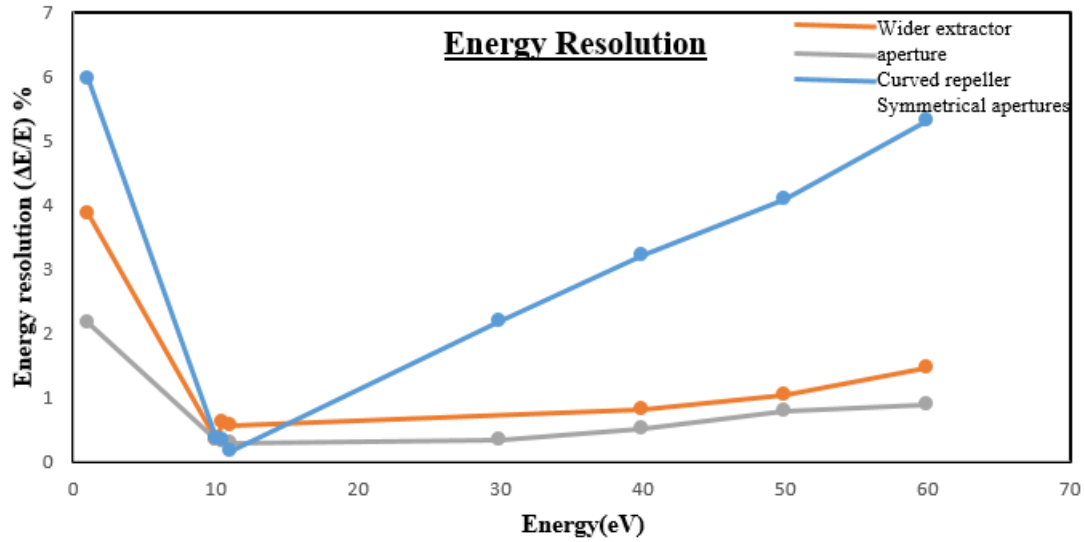
Chapter 4

Design implementation

After understanding the working of various electrode configurations and studying the energy resolutions for each one of them, the next piece of work to perform was providing it a mechanical framework and testing its practical limitations. As far as the theoretical framework of the simulations was considered, the tested configurations were working fine, but certain limitations regarding their implementation were overlooked which are discussed in detail in this chapter.

4.1   Proposed design

Based on the analysis performed in the previous chapter, I figured out that the circular electrode plates are best suited according to the chamber dimensions and resolution requirements. Along with this, considering the ratios of aperture diameters for extractor and ground plates, it was found out that rather than keeping the extractor and ground plate apertures in a decreasing manner if we keep the inverse, then it significantly increases the energy resolution and enhances the focusing conditions. This effect is further intensified with the usage of a curved repeller plate which eventually decreased the curvature of the image plane and resulted in comparatively better-focusing conditions. Therefore, a best possible choice to move on with the simulations is the one with the curved repeller plate and a bigger extractor aperture which collectively constitutes a plano-convex lens kind of lensing conditions due to

the inter-penetration of repeller and extraction fields and modifies the equipotential surface contours. But as the extractor aperture was widened more and more, it required more voltages on the electrode plates to push the particles further. It resulted in more concern towards the pressure building up conditions inside the chamber due to the usage of a continuous molecular beam source which might have resulted in gas discharge problems at certain threshold levels and demanded immediate attention to get rid of.

4.2 Problems

1. **The Paschen's law:** It is an equation which provides the breakdown voltage to initiate an electric discharge in gas between two electrodes as a function of pressure and gap length. The relation as studied by him follows:

   - Keeping the gap length constant, the voltage necessary to arc across the gap is found to decrease as the pressure is reduced and then increase gradually, exceeding its original value.

   - Keeping the gas pressure constant, the voltage needed to cause an arc reduces as the gap size is reduced but only to a point. The voltage needed to produce an arc begins to rise and again exceed its original value as the gap is decreased further. The voltage is a function of the product of the pressure and gap length only for a given gas.

   Paschen found a curve to illustrate the relationship between voltage and pressure-gap length product, called Paschen's curve.

   He found an equation that fit these curves,

   $$V_B = \frac{B(pd)}{ln(A(pd)) - ln(ln(1 + \frac{1}{\gamma_{se}}))}$$

   where V is the breakdown voltage in volts, p is the pressure in pascals, d is the gap distance in meters, γ_{se} is the secondary-electron-emission coefficient (the number of secondary electrons produced per incident positive ion), A is the saturation ionization in the gas at a particular E/p (electric field/pressure),
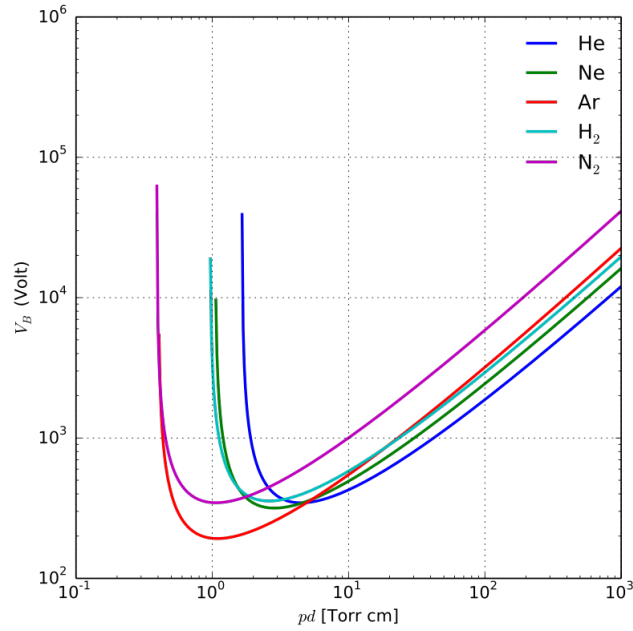
Figure 4.1: Paschen curves obtained for argon, helium, neon, hydrogen and nitrogen [Wikipedia contributors 18].

and B is related to the excitation and ionization energies. This equation is known as Paschen's law. At higher pressures and gap lengths, the breakdown voltage is approximately proportional to the product of pressure and gap length, and the term Paschen's law is sometimes used to refer to this simpler relation.[Wikipedia contributors 18]

Here, we intend to use stainless steel for the manufacturing of electrode plates, and the Paschen curve for it in combination with argon gas is shown below:
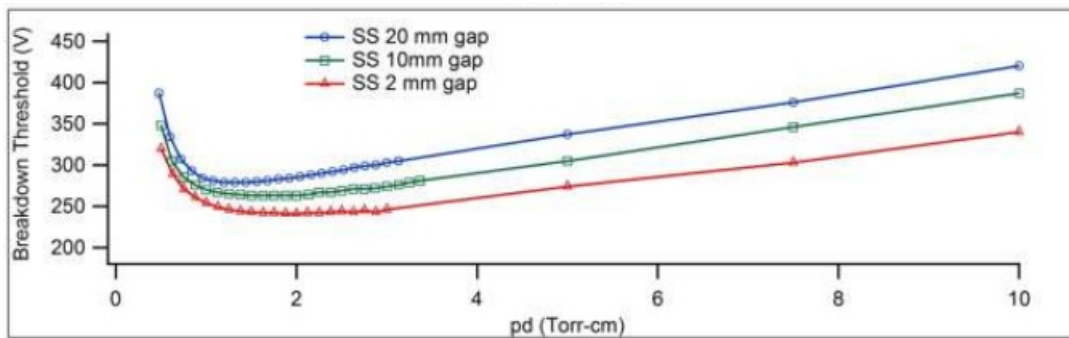

Figure 4.2: Paschen curve for argon with stainless steel electrodes [Steven Adams]

Based on the curve above, the VMI geometry needed to be configured again.

2. **Unwanted Scattering:** To prevent any kind of additional noisy signals on the detector, scattering of photons(IR, XUV) striking from different parts of the

spectrometer needs to be avoided. Thus, to take all preventive measures, we didn't want the beam diameter at the entrance of the electrode plates to be comparable to the distance between them. A rough estimation was done based on a tentative size guess of the plates which was taken to be 12 cm. So, from center of the plates to the edges, we have a distance of 6 cm, which is considered as the point of interest for the calculations given below.

Using, $z_R = \frac{\pi \omega_0^2}{\lambda}$ and $\omega^2 = \omega_0^2 \left[1 + \left(\frac{z}{z_R}\right)^2\right]$, where z_R is Rayleigh range of the beam, z is the distance from beam waist, ω is beam diameter, $\omega_0 = 50 \mu m$ is beam waist and λ is laser wavelength, we found out that-

for He-Ne:

$z_R = 2.43 mm$

$\omega(6cm) = 369.36 \mu m$

for IR:

$z_R = 9.82 mm$

$\omega(6cm) = 133.3 \mu m$

And apart from this, there should be enough space between VMI and outer chamber walls with a margin of putting a μ metal shield around to evade deflections of particle trajectories due to external stray magnetic fields, so that unwanted scattering could be avoided as far as possible.

3. **Gas injection into the system:** After studying various possibilities of placing a gas jet for the injection of target gas into the interaction region, it was noted that the best-suited place for the aforementioned is below the repeller plate similar to an integrated gas injection system described in [O ch]. The preliminary idea for that was to use a veterinary hypodermic needle having an orifice diameter of 700 μm and pass it through a hole of around 5mm in repeller plate. A wider hole diameter is chosen to take into consideration the thickness of the walls of the needle, an insulating coating over its surface to avert the high potential field lines due to voltages on the electrodes and give it some space for its movement to align it properly at the focus of the XUV beam in the interaction zone. But this integrated system could be of substantial damage in continuous mode to the micro-channel plate(MCP), the detector, in line to the axis of the spectrometer if the pressure shoots up above a certain threshold level and the gas would be directly hitting the detector. The pressure inside the chamber with the use of a turbo-molecular pump is maintained at around 10^{-7}

mbar, and on injecting the target gas, it would be in the range of $10^{-4} - 10^{-5}$ mbar. Above this pressure range, it would harm the MCP.

To take care of this, it was anticipated to make use of a home-made pulsed gas jet valve as the target gas source. Further details regarding which are contained in the next chapter.

4.3 Rectification

The above-mentioned problems were analyzed and a new design to keep in line with the solutions was simulated. It was noted that a thin and compact lens(electrode spacing around 1 cm) design was required to avoid problems related to Paschen's law whereas assembling and scattering problems required a thicker geometry (electrodes spacing 2 cm or more).

As mentioned above, Paschen's law required a thin lens geometry with a compact electrode configuration. This reduces the high voltage requirements to nominal ones with a shorter time-of-flight(TOF) length. As a consequence, the initial notion of implementing VMI with TOF was kept aside as TOF demands a longer tube length (i.e., the distance between ground and detector should be 1 foot or more for obtaining a good time resolution between the arrival times of different fragments). It was decided not to increase the chamber length further and place the MCP over the chamber head in the present condition as it is. A zero length flange is a desideratum for placing the MCP overhead on the chamber as the MCP is a flanged one with a CF150 flange and the VMI chamber top is a CF200 cap. Thus, moving further the first step was to fix the distance between the interaction zone dictated by laser height on the table and the detector. Then, the extractor and repeller plates were kept at equal distances from the passing line of the laser beam and the overall distance between them were adjusted to achieve a good focusing.

The chamber drawing is given in Fig.4.3 whose careful study was a prerequisite for considering all the finer details in configuring the design.
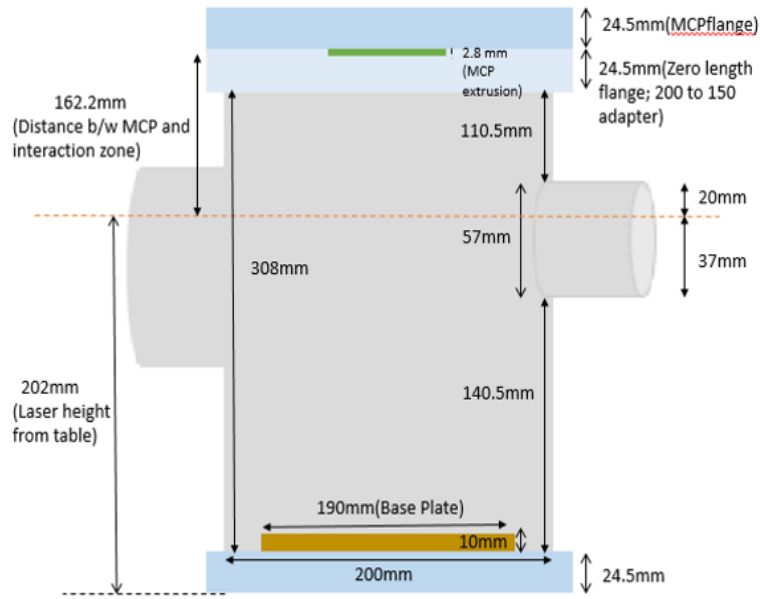
With this, to keep unwanted scattering under control and assembling a bit easier, I,

Figure 4.3: VMI Chamber dimensions

later on, kept the electrode spacing to at an optimum of 2 cm.

To resolve the gas injection problem, several positions to place the nozzle of the gas jet were tested. It was found out that the nozzle shouldn't be placed anywhere inside the electrode plates because that was distorting the electric field contours very much, thereby, the immersion lens. After this, the idea of an integrated gas injection system with the repeller plate was conceived. For the gas injection, a small hole of 5mm is made through the repeller plate with a small extension at the back of the plate to guide the capillary throughout and not distort the field contours which create the immersion lens. There too, if it was kept just 1 mm above the repeller plate, it was misshaping the field lines. So, it was decided to keep the nozzle a bit beneath the repeller plate for keeping the electric field lines intact to form the focusing lens. An illustration for the same is shown in Fig.4.4

The final simulation based on all these considerations is shown below and is tested for its resolution which is shown in Fig.4.5

30
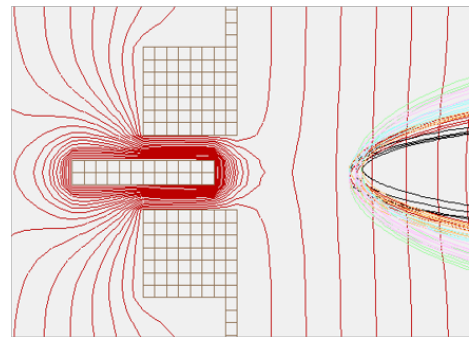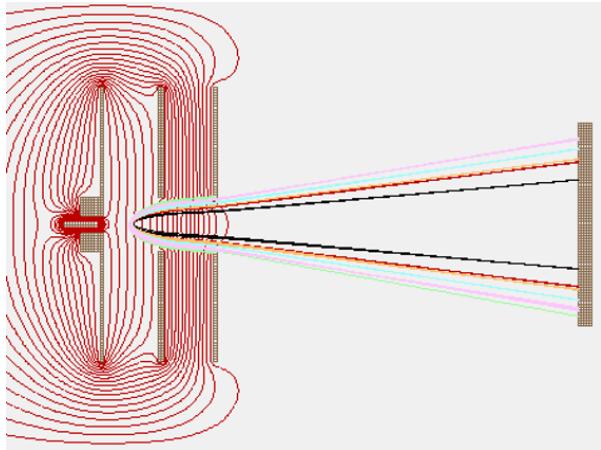
(a) The gas jet nozzle beneath the repeller plate
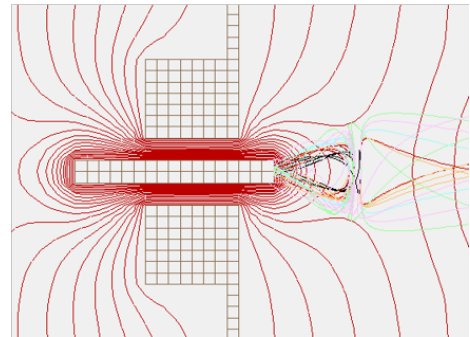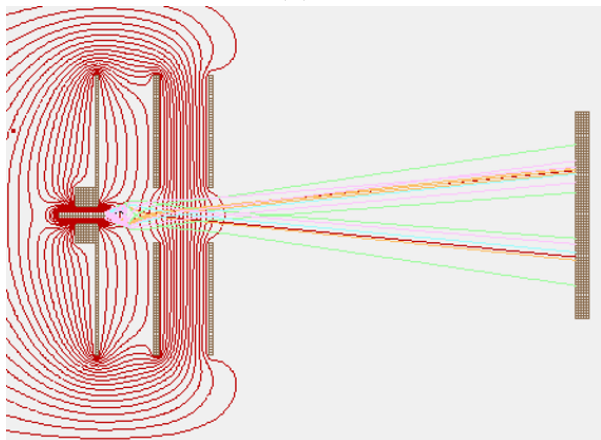
(b) The gas jet nozzle over the repeller plate

Figure 4.4: Scrutinizing the VMI design for an appropriate position to place the gas jet nozzle
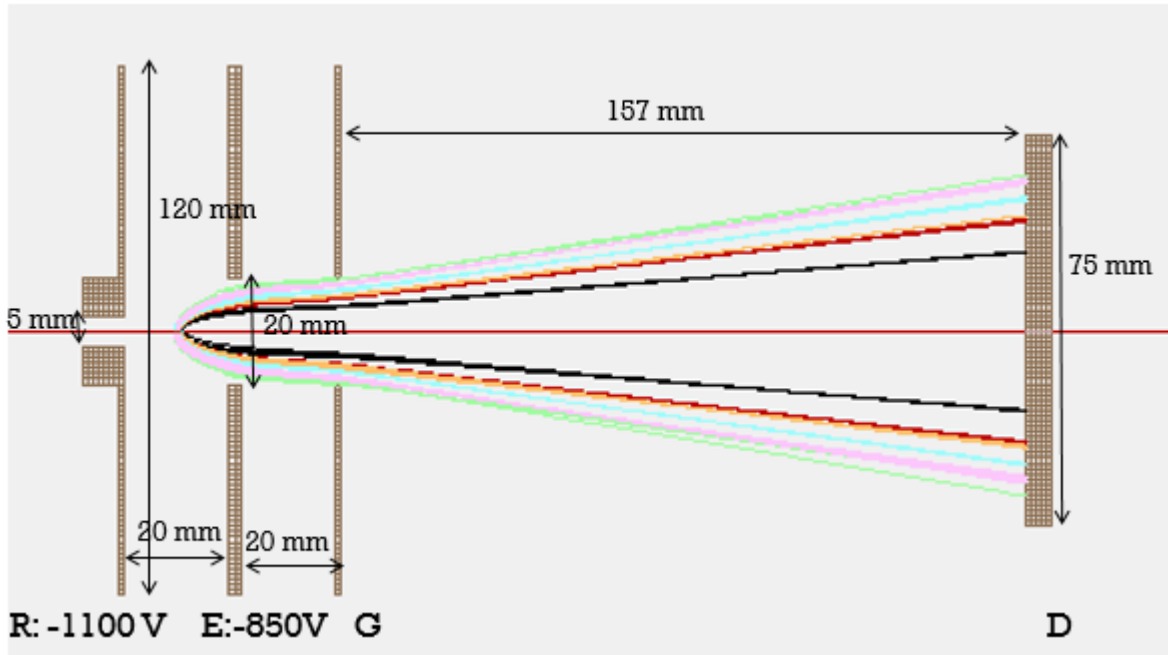
(a) The final SIMION design

Energy (eV)	Resolution ($\Delta E/E$) %
5	0.8988
10	0.5844
11	0.4442
15	2.7513
20	4.5962
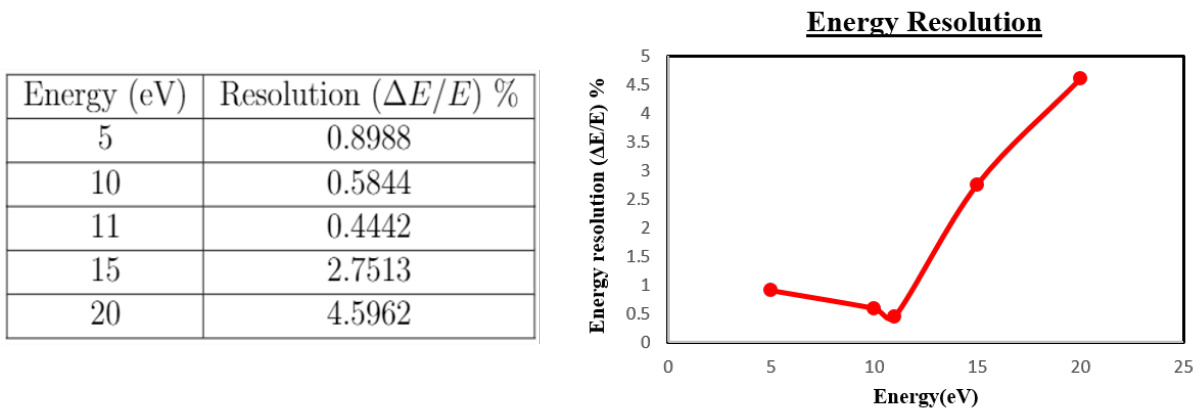
(b) Energy resolution of the final simulated design

Figure 4.5: The final design for VMI to be constructed

4.4 Model

The above-simulated configuration was given a mechanical framework in SolidWorks, and a 3D CAD model was made as follows.

Figure 4.6: The SolidWorks 3D CAD model

The various parts and models in finer details are described below:

1. **The Repeller Plate:** Stainless steel plate of thickness 1mm with a hole of 5mm in the center for capillary integra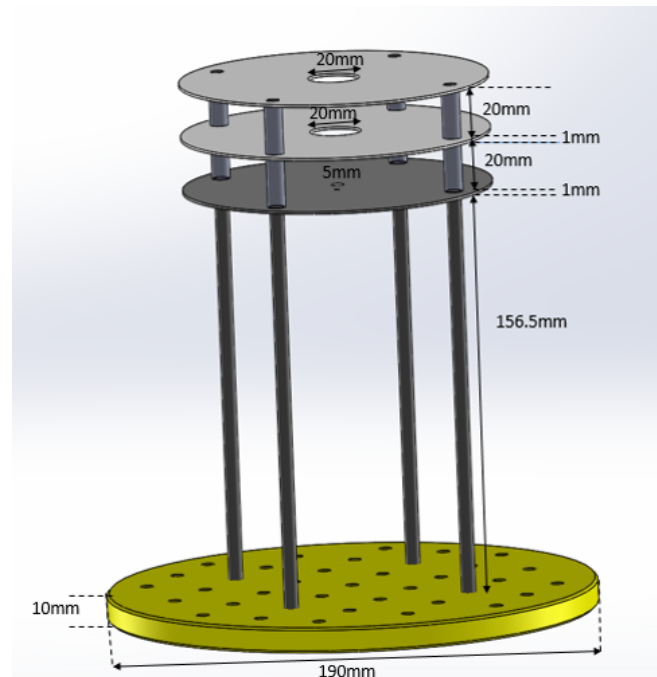tion. A small extension to be manufactured together or attached below the repeller plate is required to guide the capillary through the repeller hole and prevent any kind of unwanted distortion of the field lines.

2. **The Extractor and Ground plates**
   Material: Stainless steel

3. **Insulating spacers**: To be placed in between the plates for bushing and separating the plates from each other.
   Material: Ceramics

4. **Standing rods:** They would provide the foundations to the electrode plates to place inside the VMI chamber and constitute the pillars of the VMI spectrom-

4 × Ø 5 ▽ 37
M6x1.0 - 6H ▽ 32

101.60mm

90°

50.80mm

101.60mm

Ø5mm

50.80mm

50.80mm

Ø120mm

9mm

Ø5mm

Ø20mm
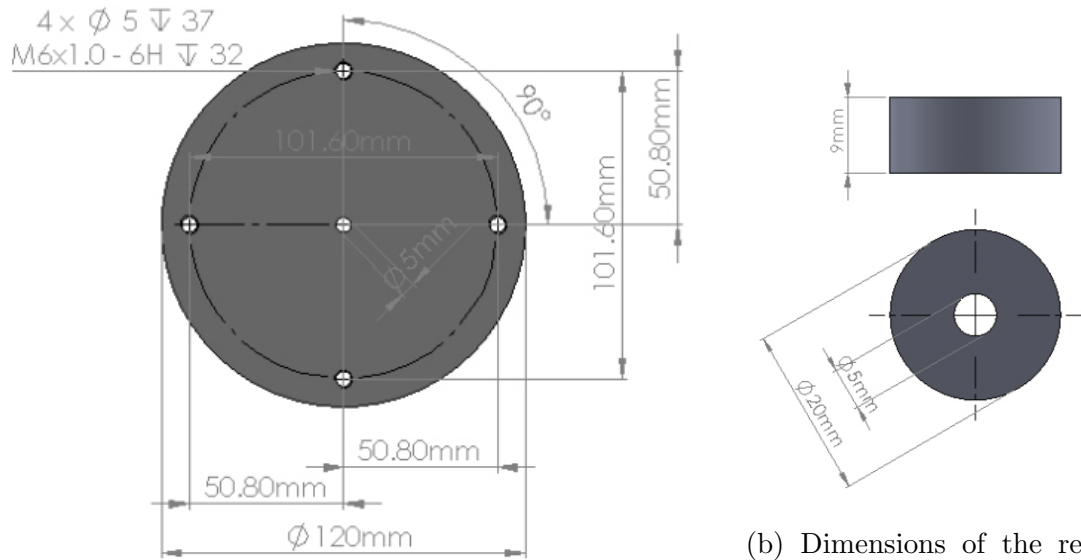
(b) Dimensions of the repeller extension

(a) Dimensions of the repeller plate

Figure 4.7: Dimensions of the repeller plate

4 × Ø 5 ▽ 37
M6x1.0 - 6H ▽ 32

Ø20mm

101.60mm

50.80mm
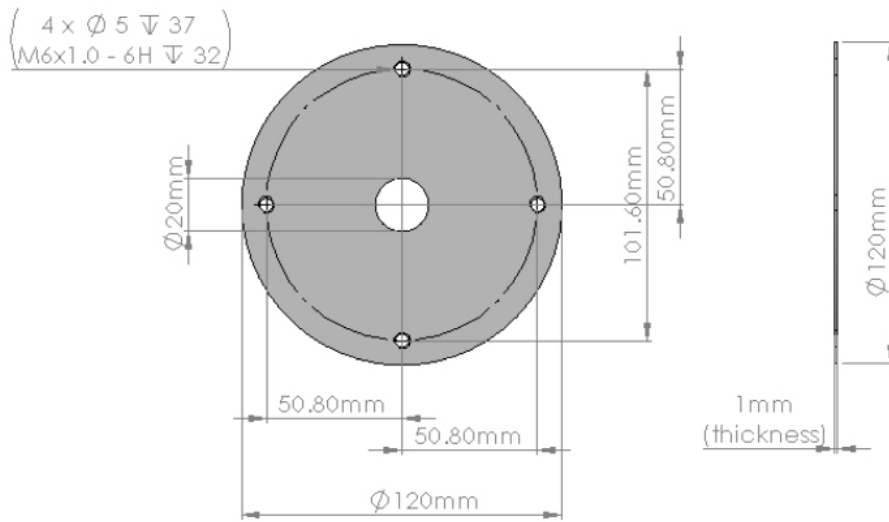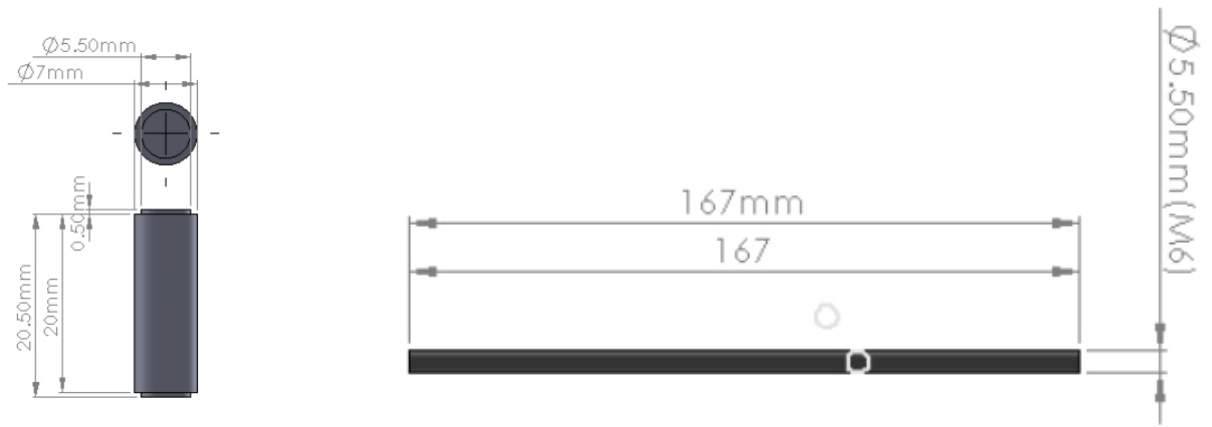
50.80mm

50.80mm

Ø120mm

1mm
(thickness)

Ø120mm

Figure 4.8: Dimension for extractor and ground plates (same for both)

eter.

Material: PTFE or Teflon

In toto, the final VMI assembly would look alike:

(a) Dimensions of ceramic bushings
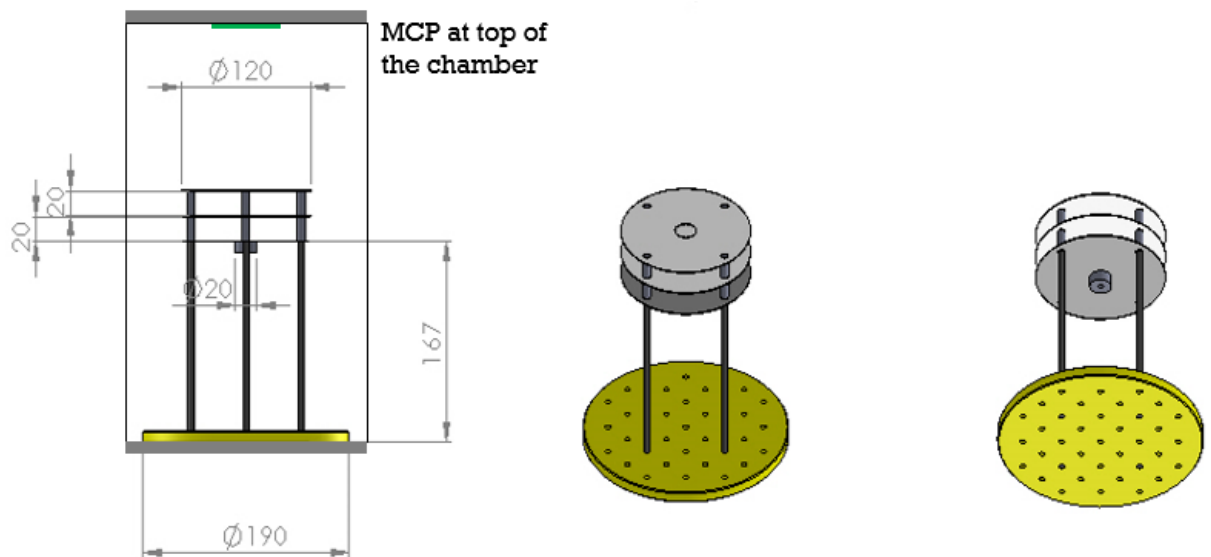
(b) Standing rods

Figure 4.9: Caging parts

Figure 4.10: Final VMI Assembly on base plate

Chapter 5

Pulsed Valve

A continuous target gas source imposes an essential constant load on the vacuum pumps. Furthermore, continuous leakage of the gas into the chamber in such experiments may contribute to a background signal limiting the detection sensitivity to photoionized products. Here, in this chapter, I have described a simple design of a piezoelectric pulsed gas valve, in which the gas flow through the nozzle orifice can be rapidly switched on or off by a piezoelectric disc on applying voltage, which would be able to mitigate these limitations for the spectroscopic experiments to be done using VMI spectrometer.

5.1   Introduction

The piezoelectric valve is actuated by a flexing disk of piezo material attached to a metallic membrane. High resonance frequencies of the disk at several kHz and low power consumption make it an ideal choice to impart pulsing of the gas at high repetition rates [Proch]. The instantaneous pulse beam intensity can be made very large compared to a continuous source by making the duty cycle small and without overloading the vacuum pumps. Also, the background signal in the detector can be reduced by a large factor because the source is open for only a small fraction of the time in association with the laser pulses.

The principle of operation of such a pulsed valve is illustrated schematically in the

Fig.5.1. It works on the principle of inverse piezoelectric effect which is described by the resulting contraction or expansion of a piezoelectric crystal along an electric axis when the crystal is under the influence of an electric field in the same direction. It will produce mechanical deformation or mechanical pressure in this direction. With the withdrawal of the electric field, this deformation or pressure will disappear as well. This type of piezoceramics is anticipated to possess a radial resonance mode with an operation frequency dependent on the ratio of the diameter and thickness of the disk. With the application of an electric potential on the piezoelectric disk, mechanical deformation is induced in the piezoelectric ceramics designed by the radial mode generation.
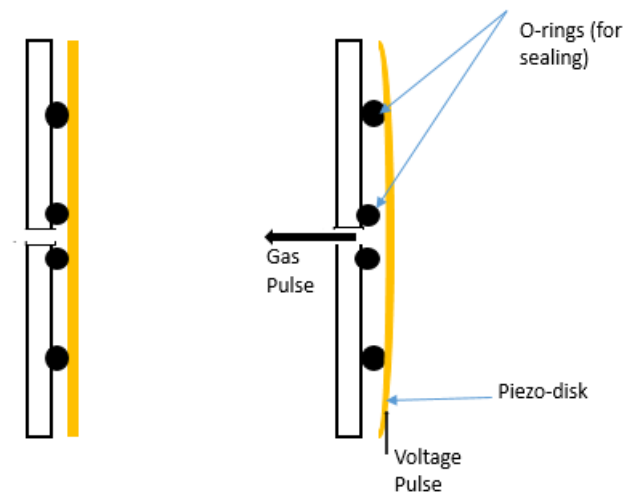

Figure 5.1: Principle of operation of piezo valve

However, there are a few drawbacks incorporated with this pulsed valve which include small excursion of the piezo disk of just a few micrometres and its poor strength. There could also be undesired multiple pulsing due to reduced damping of the membrane. A limited useful pressure range does not allow a reduced flow restricted by nozzle diameter to be compensated by pressure increase. The total force produced by the crystal upon opening is small, thus a large nozzle diameter and high backing pressure might not give a linear throughput, $Q = p_0 d_0^2$ as a function of backing pressure due to the insufficient opening of the valve at high pressures. Non-linearity does not show up immediately, indicating that the force produced by the crystal is comparable to that produced by the gas at the orifice. For larger orifices and higher pressures, one can simply increase the driving voltage on the crystal to produce a larger opening and

extend the linear response region. [Cross]

5.2 Design and working

I started with the calibration of the piezoelectric disk as there were no information available of its working range to get a follow up on its working with the implementation of a Michelson Interferometer setup whose schematic is shown in Fig.5.2a. It was necessary to see whether the displacement is having a linear response with applied voltage or not. The piezo disk was given a varying voltage (tested with different waveforms, e.g. sine, square, ramp, triangular, dc etc.) and a speckled interference pattern was observed on the screen. A photodiode was later on fixed at the center of the speckled interference pattern, and the output was connected to an oscilloscope. Based on the number of fringe count in a voltage pulse half-cycle, the displacement of the piezo disk was calculated with varying voltage using the formula given below:

$$d = \frac{N\lambda}{2} \tag{5.1}$$

where, d is the displacement of the piezo disk, N is the number of fringes in a pulse half-cycle and λ is the wavelength of the laser used.
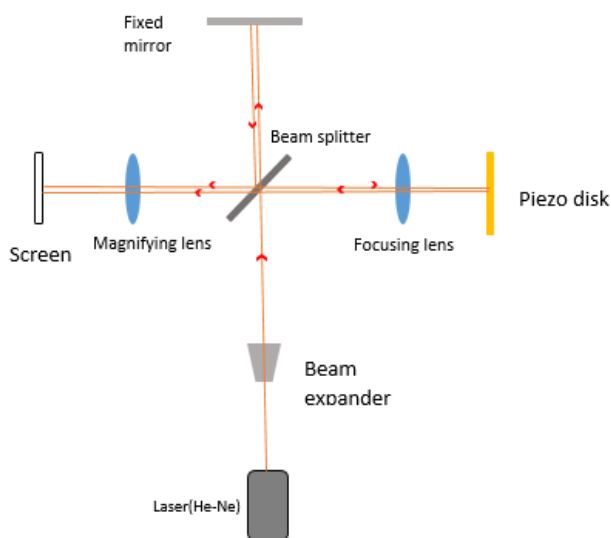
(a) Michelson interferometer setup used for the calibration of the piezo disk
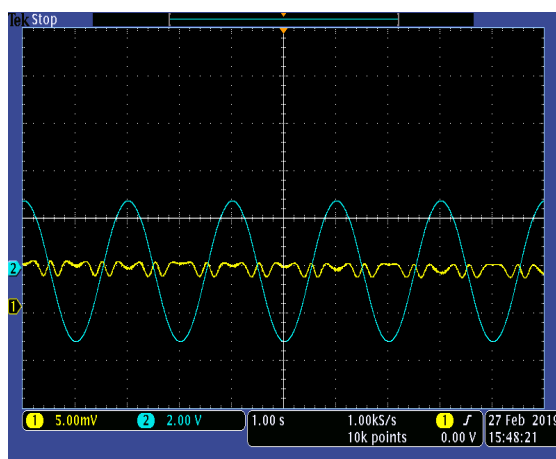
(b) Oscilloscope data for sinusoidal pulse with 3V amplitude

Figure 5.2: Piezo-disc calibration setup

A function generator was used to provide the piezo a sinusoidal waveform with varying amplitude from 1 V to 10 V (the maximum of the function generator), at a frequency of 500 mHz for data collection. The resulting fringes were recorded using a photodiode as shown in Fig. 5.2b. The blue curve shows the output pulse from the function generator and yellow curve indicates the emerging and collapsing of interference fringes in time. The data is collated as below:

Voltage (Volts)	N	d (nm)
1	0.625	395.5
2	1.25	791
3	2	1265.6
4	2.5	1582
5	3	1898.4
6	3.5	2214.8
7	4	2531.2
8	4.75	3005.8
9	5.4	3417.12
10	6	3796.8

Table 5.1: Measurements taken using Michelson interferometer

A graph is plotted between voltage and displacement as shown in Fig.5.3b The graph
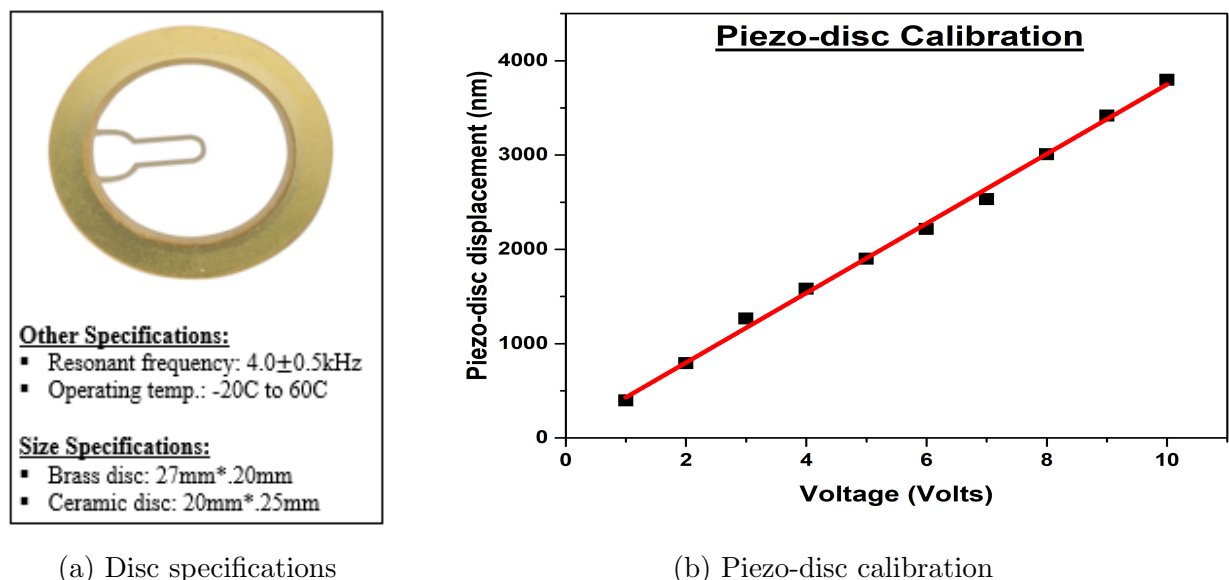
(a) Disc specifications

(b) Piezo-disc calibration

Figure 5.3: Piezo-disk specifications

shows a linear behaviour of displacement of the piezo disc with a varying voltage which suits well with the desired conditions. The voltage can be increased further

till 90 V for feeding the piezo disk which is not done here due to a limited range of operation of the function generator used. But as can be seen here, the displacement amplitude achieved here till 10 V is a few microns ($3.8\mu m$ in this case), which could achieve a maximum of ten microns with this disc with a voltage of 80-90 V. This small displacement might cause problems while working as the amount of gas to flow outside during a pulse would be limited and would cease in some cases. This can't be compensated by a high backing pressure which too has an operational limit as described above which might result in breaking of the piezoceramic as well.

The pulsed valve seal is made by the piezo disk itself clamped at the edges on the inner hollow cylinder and resting on viton O-rings in the center without any external voltage. On applying voltage to the piezo disk, the disk can be flexed sufficiently to break the seal on the center O-ring and allow gas to flow out through the center hole of 1 mm, which can behave as a nozzle for the hydrodynamic expansion. The force required to flex the disk would be provided by a pulse generator to cause deformation along with the thickness in the piezo disc, resulting in opening the pulse. The magnitude of the deformation will depend on the amplitude of the driving pulse. The valve disk would be set in the closed position in the absence of any kind of external field, i.e., not exerting any force on the O-ring in the center. On application of an electric pulse, the disk will start deforming along the thickness, allowing gas to flow through the hole, reaching its maximum amplitude of displacement and again coming back to its initial position after the pulse, will collide with the O-ring seal and stop. Amount of force applied on the disk should be sufficient to allow unrestricted flow of the gas to outside. A design implementing this idea is made in SolidWorks which is shown in Fig.5.4. The volume available inside the chamber to build up the gas reservoir is $16.85cm^3$.

When the mechanical motion of the piezo disk would be sufficiently fast, the duration of the gas pulse will depend not only on mechanical parameters, but on the rate at which the gas flow becomes organized and directed through the nozzle, and at the rate at which gas is ejected which remains in the nozzle as the valve closes[Gentry].
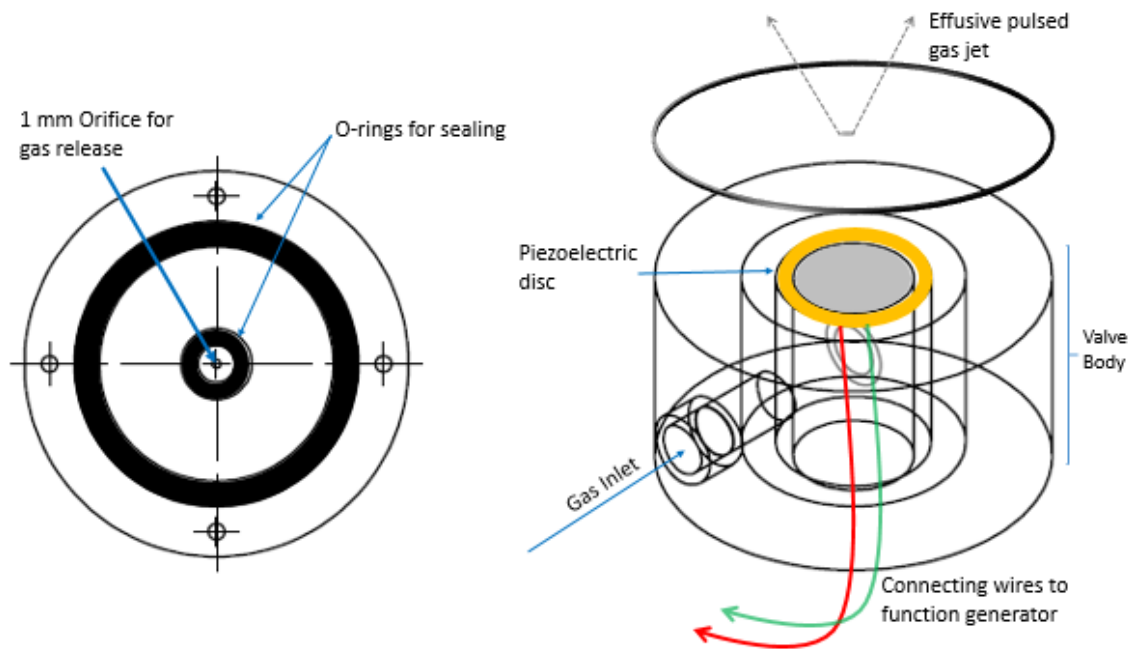
Figure 5.4: The piezo-disk valve design drawings in 2D
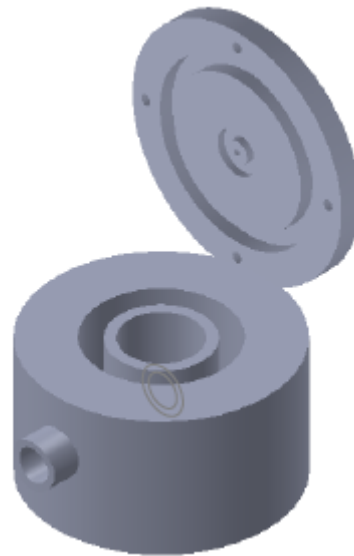
Figure 5.5: The valve body in 3D made in SolidWorks

5.3 Testing and Observations

The designed piezo-disk valve was fabricated into a prototype using 3D printer for testing purposes into its final form as shown in Fig.5.6 and the rest of the components were attached with it. The 3D printer uses a thermoplastic filament for fabrication. The piezoelectric disk was glued to the inner hollow cylinder taking the connecting wires out through it and a rubber pipe was joined to to the gas inlet port. Two

O-rings are placed in the top plate one for making the whole chamber leak tight and other in the center to act as the piezo-disk seat for pulsing purposes.
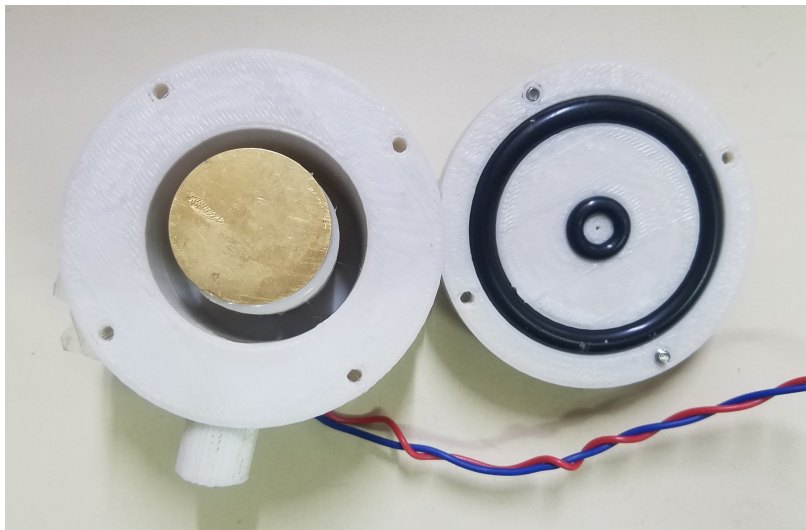

Figure 5.6: A 3D printed prototype of the model

Testing:

The first step was to test it for leaking and later for the pulsing action by the piezo-disk. To test for leaking, first I tried to fill the whole chamber with smoke to examine for all the leak points as it could be a good indicator giving precise information. But I couldn't build up much pressure inside the chamber. After that, I used a bicycle pump for the purpose. The whole system is shown in Fig.5.7.

Figure 5.7: Testing leakage with a bicycle pump

By filling the chamber with gas using the bicycle pump, it was figured out that the chamber was not able to sustain much pressure inside it and the gas filled leaked from

all the edges of the outer O-ring and from the center nozzle part also. The pressure inside the chamber made the top plate to levitate above the valve body and allowed the passage of gas through it. When the top plate was made to held more tightly with the chamber body by tightening the assembling screws with further pressure to make a proper grip between the outer O-ring and the upper chamber face, the material from which it was made started breaking up. Moreover, the 3D printing filament is a soft material and the model fabrication density is quite low in accord with the mesh size limit of the 3D printer, so high pressure can't be build inside that. It would have high degassing, so doesn't suit for an ideal choice to be used inside a vacuum chamber as required by the whole other VMI setup. Further testing was brought to a halt subsequently. For testing the pulsed valve working via the mentioned design, an ideal choice would be to manufacture it with some vacuum compatible material such as stainless steel. It could be brought into implementation only after that.

Chapter 6

Conclusion and Future outlook

A VMI design is simulated in SIMION and tested for its suitability to fit inside the attosecond-XUV VMI chamber. The resolution limit achieved in the design as of now is around 1% for particles in the energy range of 0-12 eV. One of the critical points regarding the resolution that can be obtained, is the interaction volume, which is considered as 1 cm^3 here. This requires a rather tight focus for the laser and a well-collimated gas jet. The focus of the beam should overlap with the gas beam. Within the region of gas-laser overlap where a signal can be detected, changing the laser alignment slightly can improve the focus of the particle beam. Therefore, this assumed limit is comparatively larger than what would be there in an actual scenario at the focus of the laser beam (the laser beam width is around $100\mu m$) and the molecular beam. Then in theory, we should expect a better particle beam resolution at the detector, but there are other experimental and assembling factors which would account for a lower resolution than the expected result.

The design is suited for electrons as well as ions of higher atomic masses, whether positive or negative. The shape of the electrodes can be varied deliberately in order to achieve a higher resolution(e.g. as shown in the simulations given in Chapter 3 and Fig.3.6, for the energies $< 40eV$ circular electrode rings are more effective whereas for energies $> 40eV$ squared ring electrodes are better). The lens can be corrected for lens aberrations such as image curvature and spherical aberrations by modifying the potential field in an asymmetric manner by using curved electrode plates or keeping the inner diameter for extractor and ground plates different as illustrated in Fig.3.8.

Desired electric field shapes are much harder to determine and create since they result from complex interactions of electrode/pole shapes, spacing, potentials and can be modified significantly by space charge.

Furthermore, the result of low voltages on the electrodes and longer time-of-flight distances is that fast fragments recoiling parallel to the plane of the detector surface are likely to spread too far and miss the detector. A possible solution for this is to use a larger MCP diameter. But this is cost prohibitive. Another one is to use much higher voltages on the electrodes, but depending on the speed of the fragments, the high voltage needed would reduce the temporal resolution by decreasing the time-of-flight of the ions. Alternatively, additional electrodes can be added in order to extend the time and the region of space in which the ionised fragments are under the influence of the electric fields.

Apart from its various advantages, one possible limitation of VMI which is hard to overlook is that it relies on cylindrical symmetry of the measured distribution and on a noisy mathematical transform (the inverse Abel) to extract "a slice" through the 3D distribution. Also, the gas density that can be maintained in the interaction region is only limited by the maximum pressure which can be tolerated in the experimental chamber limited by the fact that an MCP detector needs to be operated at a high gain in the chamber.

6.1 Future outlook

The work requires assembling the set up in the laboratory and integration of all the parts for collective working. The next task would be to calibrate the setup for future use using some known energy-momentum studies results, eg. investigating the photodissociation of diatomic molecules of known dissociation channels and fragments. This would be followed by the development of image acquisition and analysis software based on our needs. The foremost image analysis method comprises of Abel transformation process for the retrieval of a slice of the 3D momentum distribution data set from a 2D image set as described in Chapter 1.

6.1.1 Applications

After the accomplishment of the assembling and calibration part of the spectrometer, the application part would be there. This will include-

- Temporal Characterization of attosecond XUV beam and developing data analysis software for calibration of attosecond pulses. This one is of utmost importance in order to move further with other experiments to perform time-resolved spectroscopic measurements using the XUV beam. The characterization of a train of attosecond pulses obtained by high harmonic generation, using mixed-color (XUV + IR) atomic two-photon ionization and electron detection on a velocity map imaging detector has been reported by [cha 6] in which the authors have shown that reconstruction of the XUV pulse shape can be performed both on the basis of sideband intensities and on the basis of the angular distribution measurements.

- To investigate the effect of line source on the process of photoionization.

- Pump-probe spectroscopy experiments, eg. amino acids spectroscopy, finding out dissociation channels for various molecular species etc.

Appendix A

Some SIMION Simulations

Apart from all the models mentioned in the thesis, there were many more models that I tried my hand on using SIMION to understand their resultant working due to geometry modifications which I have delineated in this section. Here, I have also shown how to define and adjust the various parameters whose knowledge is necessary to work in SIMION to design a VMI.

A.1   Defining particles

A sample particle definition file in SIMION looks like the following:

```
   particles {
 coordinates = 0,
 standard_beam {
   n = 5,
   tob = 0,
   mass = 0.000548579903,
   charge = -1,
   ke = 5,
   cwf = 1,
   color = 0,
   direction = vector(0, 1, 0),
```

```
    position = vector(171, 0, 0)
},
standard_beam {
  n = 5,
  tob = 0,
  mass = 0.000548579903,
  charge = -1,
  ke = 5,
  cwf = 1,
  color = 0,
  direction = vector(0, 1, 0),
  position = vector(171.5, 0, 0)
},
standard_beam {
  tob = 0,
  mass = 0.000548579903,
  charge = -1,
  ke = 5,
  cwf = 1,
  color = 0,
  direction = vector(0, -1, 0),
  position = vector(170.5, -0.5, -0.5)
},
standard_beam {
  tob = 0,
  mass = 0.000548579903,
  charge = -1,
  ke = 10,
  cwf = 1,
  color = 1,
  direction = vector(0, -1, 0),
  position = vector(171, 0, 0)
```

```
  },
  standard_beam {
    tob = 0,
    mass = 0.000548579903,
    charge = -1,
    ke = 10,
    cwf = 1,
    color = 1,
    direction = vector(0, -1, 0),
    position = vector(171.5, 0, 0)
  }
}
```
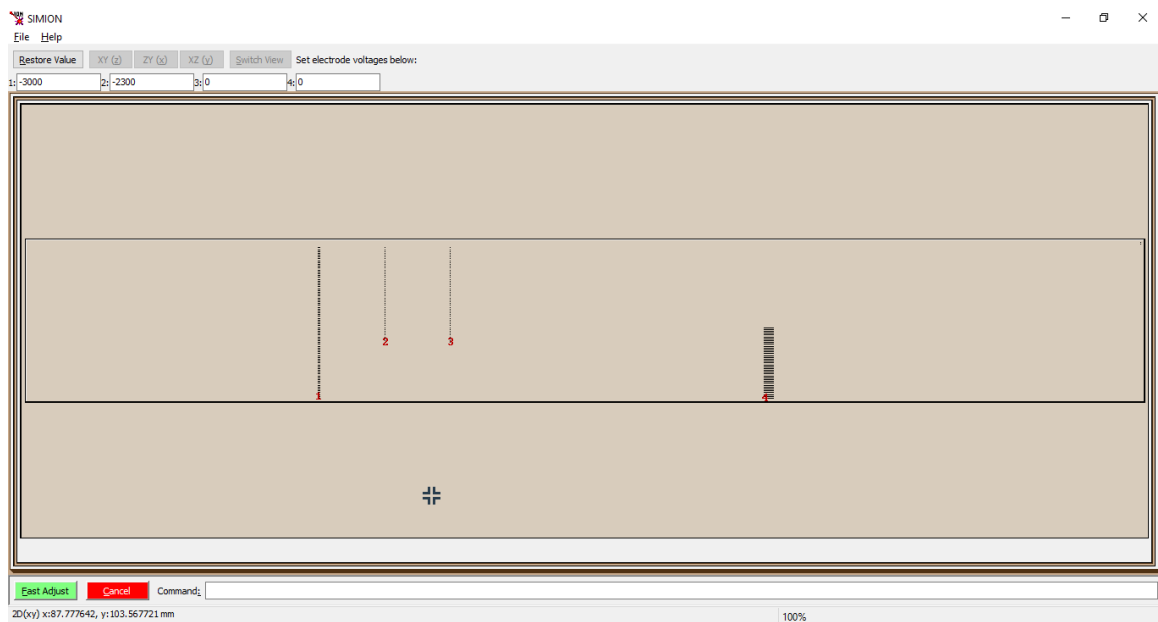
A.2 Fast Adjusting Voltages

Figure A.1: Defining electrode potentials in SIMION
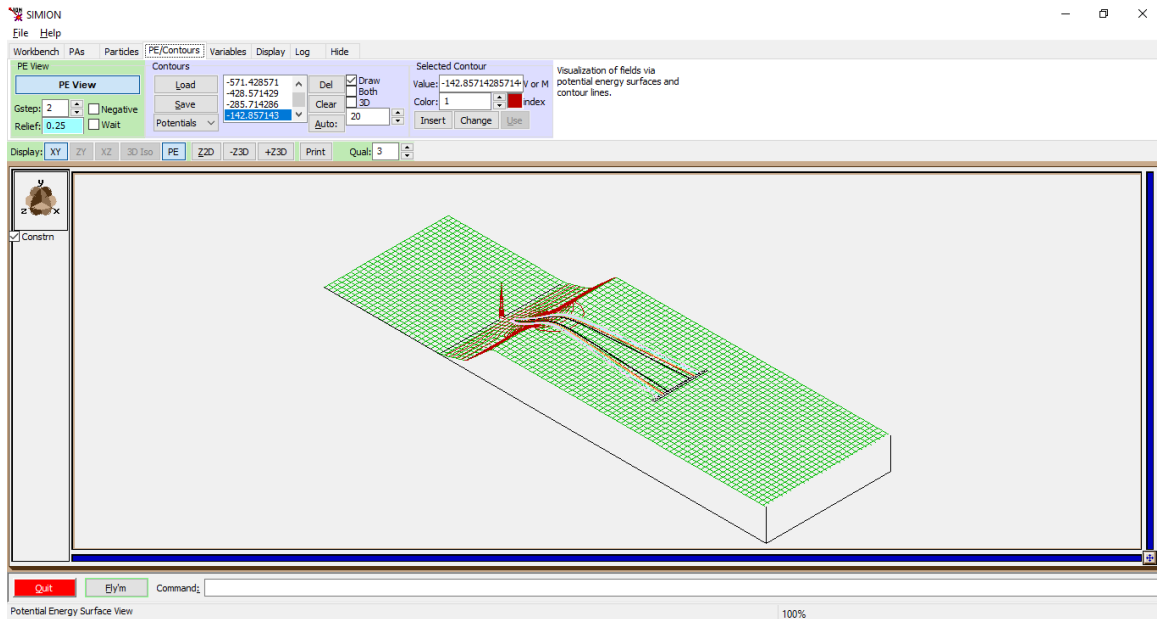
A.3   Viewing Potential Energy Surfaces

Figure A.2: Potential energy surface view

A.4   Remodelling of VMI designs discussed in literature

I have described a few models discussed in literature and remodelled them in SIMION to understand their design in a better manner.
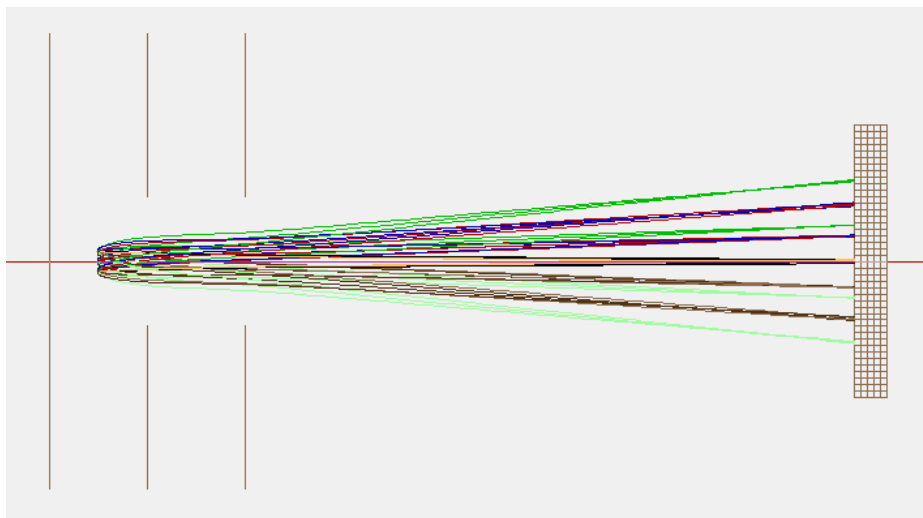

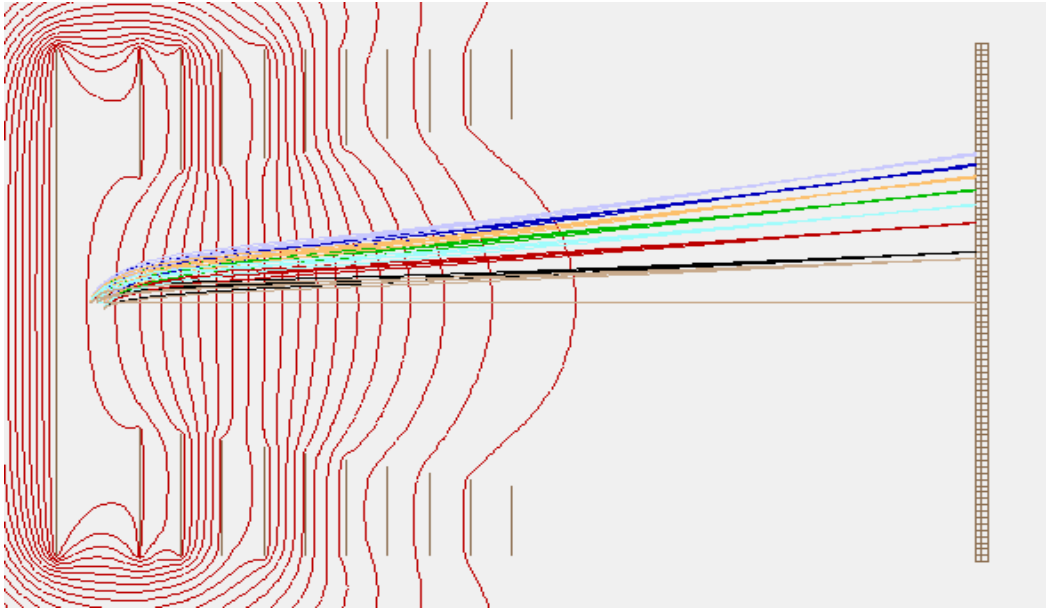Figure A.3: Eppink and Parker design modelling[Eppink 97]

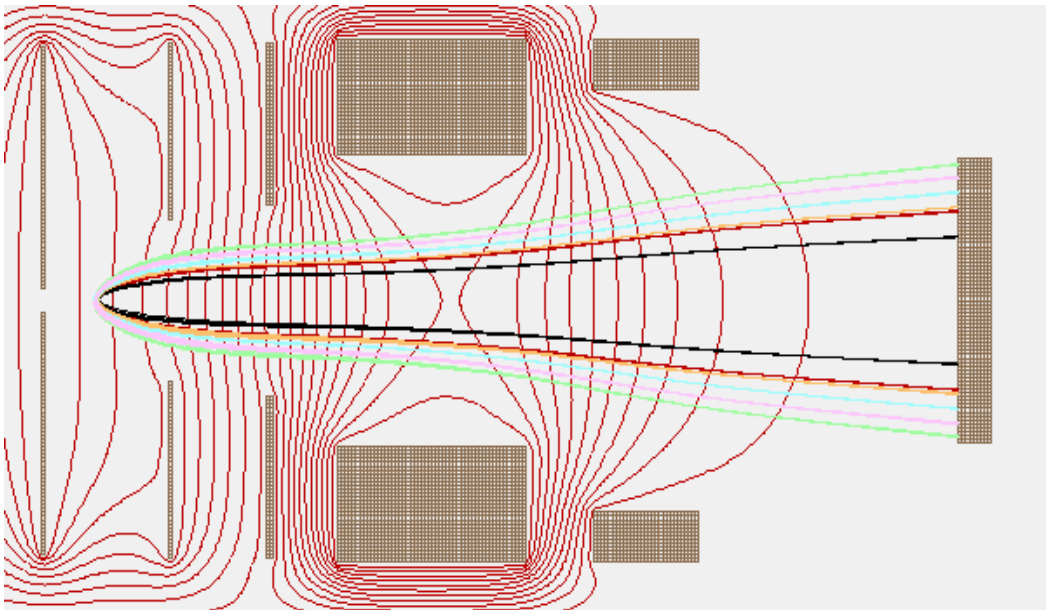Figure A.4: Thick-lens design modelling[Kling a]

Figure A.5: An extended VMI lens design modelling[Schomas1]

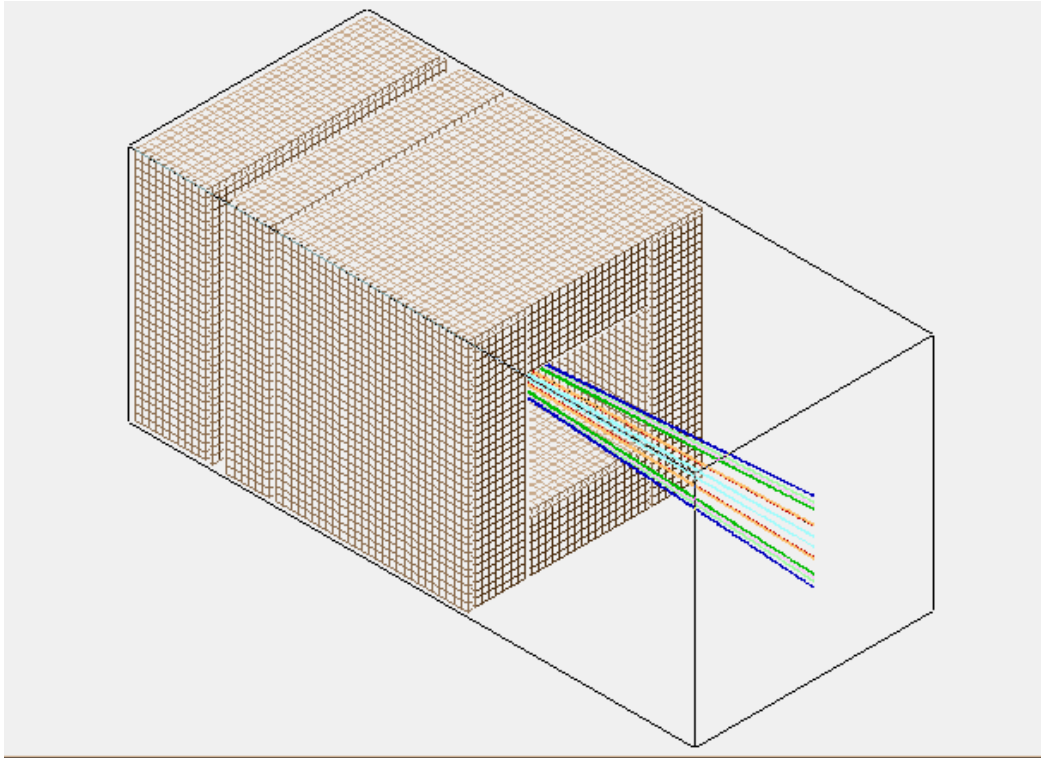## A.5 Effect of varying VMI defining parameters

Figure A.6: VMI with tube electrodes: *An immersion lens similar to one with thin electrodes plates was observed*
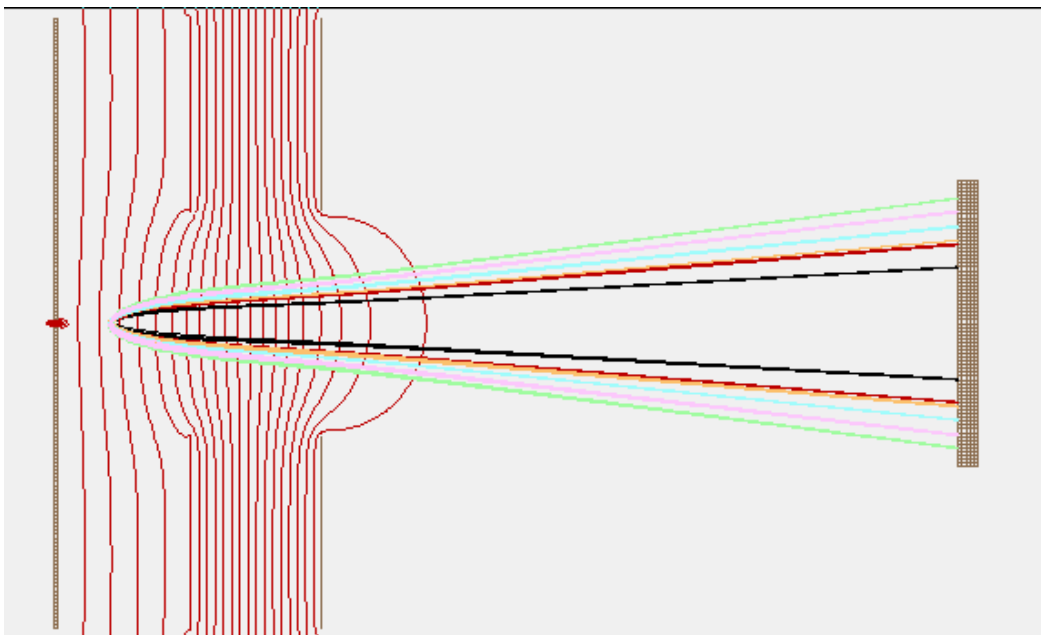

Figure A.7: Effect of greater distance between VMI plates: *Required higher volatages for focusing*

Bibliography

[10. 1]   *High-order Harmonic-generation cutoff.* Physical Review A, 1993/11/01/.

[AH 00]   Zewail AH. *Femtochemistry: Atomic-Scale Dynamics of the Chemical Bond Using Ultrafast Lasers (Nobel Lecture) Copyright((c)) The Nobel Foundation 2000. We thank the Nobel Foundation, Stockholm, for permission to print this lecture.* Angewandte Chemie (International ed. in English), vol. 39, 2000.

[cha 6]   *Attosecond Angle-Resolved Photoelectron Spectroscopy.* Physical Review Letters, vol. 91, no. 22, 2003/11/26/.

[Chandler 87]   David W. Chandler & Paul L. Houston. *Two-dimensional imaging of state-selected photodissociation products detected by multiphoton ionization.* The Journal of Chemical Physics, vol. 87, no. 2, pages 1445–1447, 1987.

[Cross]   Jon B. Cross, & James J. Valentini. *High repetition rate pulsed nozzle beam source.*

[D. Manura 08]   D. Dahl. D. Manura. *SIMION (R) 8.0 User Manual.* Scientific Instrument Services, Inc. Ringoes, NJ 08551, January 2008.

[Dasch]   Dasch. Applied Optics, Vol 31, No 8, March 1992, Pg 1146-1152.

[Eppink 97]   André T. J. B. Eppink, & David H. Parker. *Velocity map imaging of ions and electrons using electrostatic lenses: Application in photoelectron and photofragment ion imaging of molecular oxygen.* 1997.

[et al. 02]   Dribinski et al. Rev. Sci. Instrum. 73, 2634, 2002.

[Gentry]   W. Ronald Gentry & Clayton F. Giese. *Ten-microsecond pulsed molecular beam source and a fast ionization detector.*

[Hansen 85]   E. W. Hansen & P. L. Law. *Recursive methods for computing the Abel transform and its inverse.* J. Opt. Soc.A2, 510-520, 1985.

[Kling a]   N G Kling, D Paul, A Gura, G Laurent, S De, H Li, Z Wang, B Ahn, C H Kim, T K Kim, I V Litvinyuk, C L Cocke, I Ben-Itzhak, D Kim & M F Kling. *Thick-lens velocity-map imaging spectrometer with high resolution for high-energy charged particles.* Journal of Instrumentation, vol. 9, no. 05, 2014-05-30///.

[Kling b]   N G Kling, D Paul, A Gura, G Laurent, S De, H Li, Z Wang, B Ahn, C H Kim, T K Kim, I V Litvinyuk, C L Cocke, I Ben-Itzhak, D Kim, M F Kling, D Paul, A Gura, G Laurent, S De, H Li, Z Wang, B Ahn, C H Kim, T K Kim, I V Litvinyuk, C L Cocke, I Ben-Itzhak, D Kim & M F Kling. *Thick-lens velocity-map imaging spectrometer with high resolution for high-energy charged particles.* Journal of Instrumentation, vol. 9, no. 05, 2014-05-30///.

[MF 08]   Kling MF & Vrakking MJ. *Attosecond electron dynamics.* 2008.

[O ch]   Ghafur O, Siu W, Johnsson P, Kling MF, Drescher M & Vrakking MJ. *A velocity map imaging detector with an*

integrated gas injection system. 2009 March.

[Proch]   D. Proch, & T. Trickl. *A high-intensity multi-purpose piezoelectric pulsed molecular beam source.*

[Schomas1]   D. Schomas1, N. Rendler1, J. Krull1, R. Richter2, & a) M. Mudrich3. *A compact design for velocity-map imaging of energetic electrons and ions.*

[Steven Adams]   K.C. Howe Vladimir Demidov Steven Adams XuHai-Huang. *Study of Effective Secondary Electron Emission in DC Breakdown of Argon with Various Metal Electrodes.*

[Thorin 04]   Sara Thorin. *Design and construction of a velocity map imaging spectrometer.* Master's thesis, Lund Reports on Atomic Physics, LRAP-327, 2004.

[Wikipedia contributors 18] Wikipedia contributors. *Paschen's law — Wikipedia, The Free Encyclopedia.* `https://en.wikipedia.org/w/index.php?title=Paschen%27s_law&oldid=862710166`, 2018. [Online; accessed 9-April-2019].

[Wituschek 16]   A. Wituschek. *Velocity Map Imaging.* Fortgeschritte-nen praktikum ii, Albert-Ludwigs-Universit at Freiburg, 2016.